Master's Thesis
Feasibility study of short-lived neutral K meson measurement in Au + Au collisions at $\sqrt{s_{NN}} = 200$ GeV at PHENIX

Masaya Nihashi
(M086916)
Department of Physics
Hiroshima University Graduate School

Supervisor : Prof. Toru Sugitate
Primary examiner : Associate Prof. Kenta Shigaki
Examiner : Prof. Yasushi Fukazawa

February 10, 2010

Contents

List of Figures

Abstract

Our final goal is to qualitatively and quantitatively study of the the Quark-Gluon-Plasma(QGP), such a matter is expected to be that quarks and gluons are no longer confined into hadrons. Quantum ChromoDynamics(QCD) predicts the QGP phase to have the number of quarks and gluons as the degree-of-freedom at high temperatures over 170 MeV (about 2 trillions K) [1]. This phase is considered to exist in the early universe where we live few dozens micro second after Big-Bang.

The Relativistic Heavy Ion Collider(RHIC) at Brookhaven National Laboratory enables us to make a variety of measurements of the QCD multi-body system with high-energy proton + proton, deutron + Au, Cu + Cu and Au + Au collisions. These are important steps toward the understanding of the equation of state of the medium created in high-energy nuclear collisions.

Measuring an interaction between scattering partons and the QGP is a effective way to understand properties of QGP. We detect scattering partons as the high transverse-momentum(p_T) particles, larger than a few GeV. If there is an interaction between scattering partons and QCD matter, scattering partons lose their energy by emitting or by emissions of gluons. As a result, high p_T particle yeild should be suppressed. We can gain the quantitative understanding of this suppression effect to measure R_{AA}; the suppression ratio of particle yield in Au + Au collisions for it in proton + proton collisions. We have gotten evidences of the formed QGP by measuring R_{AA} of high p_T hadrons at RHIC [2].

My objective is a study of the phenomenon of strange quarks in the QGP with the measurement of R_{AA} of short-lived neutral K meson($K^0{}_S$) via 2 π^0 decay mode, the measurement of the R_{AA} means to clarify the energy loss of fast strange quarks and the presence or absence of the jet-conversion which is the processes that jets couple to chemical properties of the QGP by comparison of neutral π meson which is consisting of up and down quark.

In this thesis, I study how $K^0{}_S$ signals look like in Au + Au collisions at $\sqrt{s_{NN}} = 200GeV$ at PHENIX before the measurement of R_{AA} of $K^0{}_S$. Specifically, I estimate the multiplicity effects and the life time effect in order to measure the peak in the invariant mass distribution with four photons from

[1] F. Karsch Lecture Notes in Physics, Vol. 583, p. 209 (2002).

[2] J. Adams et al. (STAR Collaboration), Phy. Rev. Lett. 91, 072304 (2003)

${K^0}_S$. High particle multiplicity generates huge backgrounds and no wonder those backgrounds interfere cluster algorithm. In addition, the mean life time of ${K^0}_S$ which is about 0.8953×10^{-10} second [3] causes the mass shift according to the p_T of ${K^0}_S$ and their specific life times. So I emphasize this feasibilty study using both simulation and real data to search the quantitative multiplicity effects and the life time effect. Finally, I report the quantitative multiplicity effects and judge a modification method in consideration of the life time effect.

[3]Particle data group(PDG)

Chapter 1

Introduction

1.1 Historical introduction

The latter half of the twentieth century saw some quests extended from *ordinary* atomic systems to those composed of nuclear matter. Most impact was that the deep inelastic electron collision experiments on protons at MIT-SLAC indicated that nucleons have an internal structure, they are built of quarks and gluons.[1] It was the first evidence for quarks as real dynamical constituents and made changes our paradigm of atomic systems. This paradigm is the quark model, the quark introduced by Gell-Mann in 1964 and the gluon with the idea of color introduced by Nambu and Han and also by Greenberg in 1965.

The field theory that describes these partons, quarks and gluons, is the quantum chromodynamics(QCD). This theory leads to the conclusion that single free quarks or gluons cannot be studied or observed in our laboratories, because they are confined by the strong interaction that binds them to each other.

Another impact in the side of theory at another extreme condition, that is the high-temperature phase, was that QCD has led to detailed investigations of thermodynamic properties of quarks and gluons, in other words, of deconfined phase "quark-gluon plasma", with implemantations of lattice formulation and the continued exponential increases in computing power.[3]

A figure1.1 is a result of lattice QCD simulations with dynamical quarks ($N_f \neq 0$). Quark masses empolyed in the figure are $m_{u,d}/T = 0.4$ for $N_f = 2$, $m_{u,d,s}/T = 0.4$ for $N_f = 3$ and $m_{u,d}/T = 0.4$, $m_s/T = 1.0$ for $N_f = 2 + 1$.

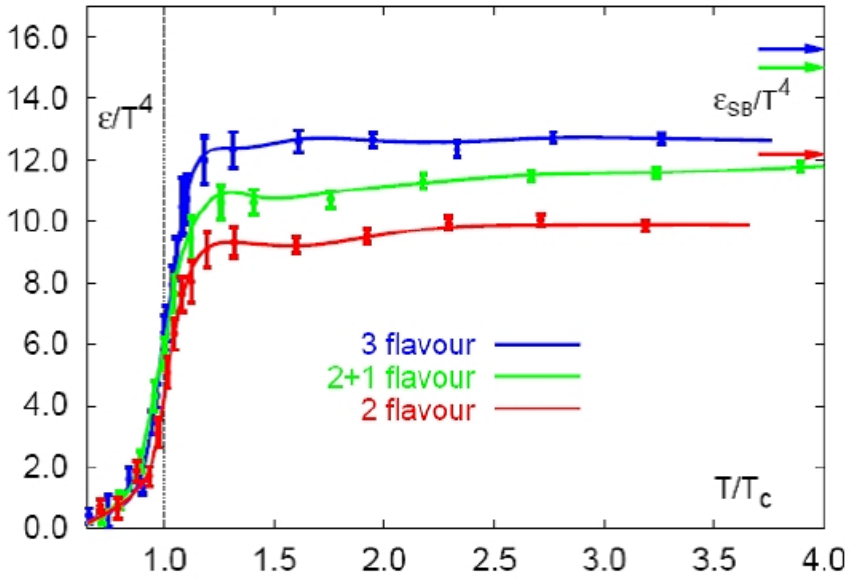

Figure 1.1: Lattice QCD[3] results for the energy $density/T^4$ as a function of the temperature scaled by the critical temperature T_C. Note the arrows on the right side indicating the values for the Stefan.Boltzmann limit.

This large change of energy density at transition temperature are seen in all three cases. The deviations from ideal gas(the Stefan-Boltzmann) limit are also seen at high temperature. At the chiral limit($m_q = 0$), the critical temperatures are found to be $T_c(N_f = 2) \sim 175$ MeV, $T_c(N_f = 3) \sim 155$ MeV. Corresponding critical energy density can be read off from the figure as $\epsilon_c \sim 1GeVfm^{-3}$. The large difference between $\epsilon_{SB}/T^4(N_f)$ and $\epsilon/T^4(N_f)$ at high temperature indicates that the gluons are still interacting above T_c.

1.2 High energy heavy ion collision

One of the ways to create QGP is thought to use relativistic nucleus-nucleus collisions. In the case of nucleus-nucleus collisions with lower energy, provided at CERN-SPS and BNL-AGS, lower temperature but high baryon density matter could be achieved. In head on nucleus-nucleus collisions such as Au+Au with $\sqrt{s_{NN}} = 200GeV$, where $\sqrt{s_{NN}}$ is center of mass energy per nucleon pair, a high energy and density matter could be produced, but low in baryon density.

1.2.1 The picture of heavy ion collisions

In ultra-relativistic heavy ion collisions the de-Broglie wavelength of the individual nucleons is so small that the nuclei can be seen as an independent accumulation of nucleons. This simplistic view implies that the Lorentz-contracted nuclei interact only in the region of geometrical overlap, determined by the distance between the centers of the two collided nuclei(b), it is called impact parameter ,see a figure1.2. The corresponding nucleons are called participants, while the nucleons outside the geometrical overlap, the spectators, are basically unaffected by the collision. We name the degree of collisions as the centrality. The most interesting phenomena of a nuclear matter is in most central collisions.

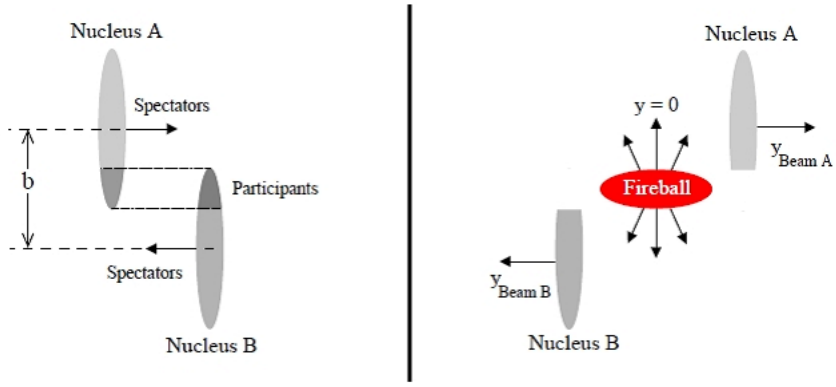

Figure 1.2: Schematic view of two colliding nuclei in the geometical participant-spectator model[15].

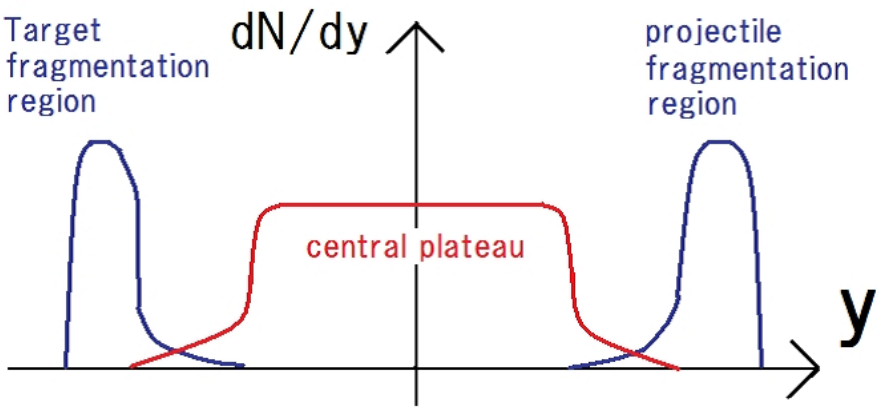

Figure 1.3: Exaggerated polt of observed rapidity distribution of generated hadrons in ultra-reativistic nuclei collisions

The participants interact with each other in the reaction zone, leading to the formation of a hot and dense region, the fireball. There are two basic scenarios for the formation of the fireball depending on the nuclear stopping in the reaction. For large stopping, described in the Landau model, the complete kinetic energy of the nucleons is converted into thermal energy and a baryon-rich fireball is formed. The characteristic rapidity distribution of produced particles in such a reaction has a maximum at mid-rapidity. In the Bjorken-McLerran scenario, the stopping is limited and the nucleons penetrate each other, they exhibit transparency. This leads to a fireball with low baryo-chemical potential as the baryon number remains concentrated near the beam rapidity. The rapidity distribution in this case should be essentially flat in the rapidity region between the two beams like a figure1.3.

In reality particles in the fragmentation regions and in the central rapidity region are not separated. Their rapidity distribution overlap[7]. In the simplest terms, we can search the properties of QGP to measure hadrons at mid rapidity region.

1.2.2 Jets

Jet production was first observed at e^+e^- colliders in 1975. The simple process for producing hadrons is;

$$e^+e^- \rightarrow q\bar{q} \tag{1.1}$$

At the center mass system, quark and anti-quark(leading partons) become charged and neutral hadrons and appear in the form of two oppositely jets. The hadrons of jets are generated around $q\bar{q}$-axis because of the potential between quarks, I mean at lager distance the potential increased indefinitely generates a quark pair and confine the quarks inside hadrons. High energetic hadrons appear from jets.

In the case of hadron-hadron collisions, parton-parton scattering can give four jets in a strict case; one from each of the scattered partons and two beam jets from the spectator partons which carry on along beam directions. As regards high p_T measurements, we give little thought about beam jets. The signature for a jet is large energy deposition in a localized area of electromagnetic calorimeter.

1.2.3 Nuclear modification factor

I will focus on what is arguably the most important result from the RHIC program: the observed depletion in the yield of high transverse momentum hadrons. Nuclear effects on single particle observables are quantifed by the nuclear modification factor, R_{AA}; suppression ratio of a particle yield in Au+Au collisions for it in proton+proton collisions.

$$R_{AA} = \left(\frac{1}{N_{evt}} \frac{d^2 N^{AA}}{dp_T dy} \right) / \left(\frac{\langle N_{coll} \rangle}{\sigma_{inel}^{pp}} \frac{d^2 \sigma^{pp}}{dp_T dy} \right) \tag{1.2}$$

This quantity is the ratio of the observed per-event yield in nuclear collisions to the expected yield. The latter is the product of the p + p cross section, $\frac{d^2\sigma^{pp}}{dp_T dy}$, and a scale factor $\frac{\langle N_{coll} \rangle}{\sigma_{inel}^{pp}}$, which is explained as fllows. If the Au + Au collisions were simply a collection of superimposed p + p collisions, the cross section for a given inelastic process would be simply be product of the total number of nucleons participating in the collision(N_{part}) and the inelastic nucleon-nucleon cross section (σ_{inel}^{pp}). The cross section for soft production can reasonably be expected to scale in such a way.

1.2.4 Jet conversion

Initially, energy loss of a leading parton had been attributed to induced gluon radiation by scattering of the leading jet parton with thermal partons from the medium. Perturbative calculations of this process yield results for R_{AA}

compatible with data after fixing one parameter characterizing the strength of the interaction, the transport coefficient $\hat{q}$ or an equivalent quantity. That is quark and gluon jets are well-defined concepts in a medium. This claim might have some validity in the case that the mean-free-path of leading parton is of the order of the size of medium, i.e. $L \leq \lambda$. Energy loss is then dominated by one gluon radiation.

However the situation is different, generally speaking. When highly energetic partons propagating through dense QCD matter, their fragmentation pattern changes in the presence of a strongly interaction medium. I mean that there is the effect not only from thermal properties,like a gluon radiation, but also from chemical properties of medium. In the processes that jets couple to chemical properties, the flavor of fragments change, for example flavor changing compton processes $q + g \leftrightarrow g + q$, annihilation and pair creation $q + \bar{q} \leftrightarrow g + g$. Measurements of identified hadrons at high pT can constrain the rate of flavor conversion. It is naturally that the energetic partons of fragments become high pT hadrons in final state. So the ratio of identified hadrons at high pT have effective information about the rate of flavor conversion. With sufficient experimental sensitivity this would lead to estimates for the mean free path λ of the jet in the medium, complementary to measurements of $\hat{q}$. Such measurements is expected to provide additional stringent tests for the validity of any model for the jet-medium coupling.

The hadrochemical composition of jet fragments changes significantly in the presence of parton energy loss. Heavier hadrons become more abundant. As seen in below figuare, for an Ejet = 50 GeV jet, the kaon to pion ratio is around 0.4, it is twice of the ratio about the vacuum jet, the proton to pion ratio is around 0.5 [4]. These medium-induced changes persist over the entire transverse momentum range. They decrease slightly with increasing jet energy, but remain clearly visible even for Ejet = 200 GeV jets.

We suggest the relative yield of strange hadrons at high p_T as a new signature for jet medium coupling. The ratio of strange quarks to the sum up and down quarks,

$$w = \frac{s}{u + d} \tag{1.3}$$

is about 5 % for the initial leading jet particle at RHIC energies at a typical pT of about 10 GeV/c. A rough estimate[5], assuming dominabce of compton channels in the initial hard scattering, would give it, the ratio of strange

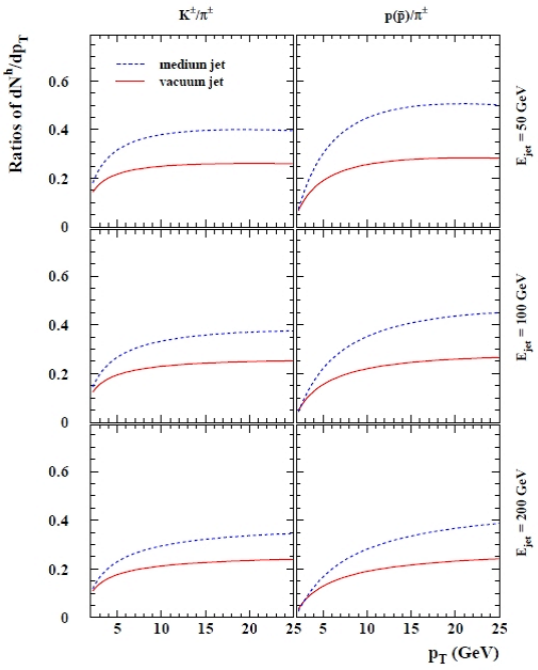

Figure 1.4: $\frac{K^{\pm}}{\pi^{\pm}}$ and $\frac{p(\bar{p})}{\pi^{\pm}}$ ratios in jets with energies $E_{jet} = 50, 100 and 200 GeV$ [4].

quarks to the sum of up and down quarks,

$$w_{jet}(pT = 10GeV) \sim w_{pdf}(x \sim 0.1, Q \sim 10GeV) \sim 6.4\% \tag{1.4}$$

However, in a chemically equilibrated QGP at given temperature the ratio is

$$w(T) \sim \frac{m_s^2}{4T^2} K_2(m_s/T). \tag{1.5}$$

assuming massless up and down quarks. For a strange quark mass of $m_s = 100MeV$ the ratio is almost half even at $T_c \sim 180MeV$:$w(T_c) = 0.47$. The difference between w_{jet} and w is rather large and we have to expect that the relative abundance of strange quark jets will rise with time.

For an infinite medium the particle ratios of jets would equilibrate to that of the medium. As another case, the same will happen to their momentum distribution, making them indistinguishable from the medium with a final

state measurement. For a finite path length L, the rate of equilibration should be a good measure of the strength of the coupling to the medium. In particular, it should give a good estimate of the mean free path λ between flavor changing scatterings. The approach to equilibrium will be determined by the ratio λ/L.

Estimation of ${K^0}_S$(short-lived neutral K meson) measurement

In this section I discuss the ${K^0}_S$ measurement at RHIC energy and LHC energy. It is obvious that the interaction of jet with medium can change the flavor of the jets, defined here as the flavor of leading parton. Nevertheless, most studies of jets in nuclear matter still focus on solely on the kinematical effects, based on quenching of longitudinal momentum and broadening of transverse(right angle against longitudinal direction) momentum of the leading parton. For example, Observable R_{AA} are sensitive to various integrals over the differential energy loss dE/dx and ultimately measure the momentum transfer per path length, commonly known as $\hat{q}$. It is summarized as the effect of jets coupling to the thermal properties of the medium. So it is so interesting that the look of flavor effect from jets coupling to the chemical properties of the medium. Measurements of identified hadrons at high transverse momentum($\mid p_T \mid$) constrain the rate of conversions. With sufficient experiment sensitivity this would lead to estimates for the mean free path λ of jet in the medium, complementary to measurements of $\hat{q}$.

A figure1.5 is the result of theoretical expectation[11] at RHIC energy. On the right-hand side it is a plot of the R_{AA} of ${K^0}_S$ as a function of p_T. we observe that conversions greatly enhance the yield of ${K^0}_S$ in nuclear collisions. In fact, conversions could lead to a R_{AA} that is up to a factor 2 larger at high p_T than that for pions or protons. A recombination contribution is not included in this study, so caution has to be exercised at lower p_T. This study predicts that the measurement of the R_{AA} of ${K^0}_S$ at high p_T will provide a unique signal for jet conversions in the QGP fromed at RHIC.

At a figure1.6 we observe that jet conversions have only a small impact on $R_{AA}^{{K^0}_S}$ at LHC energy. This had to be expected, because initial jet production is gluon dominated and strange quark jets are not very much suppressed to begin with, very unlike the situation found at RHIC. The impact of jet conversions on the R_{AA} of ${K^0}_S$ is similar to the effect on pions at LHC. We conclude that strange hadrons might no longer be a good probe of jet conversions at LHC energy.

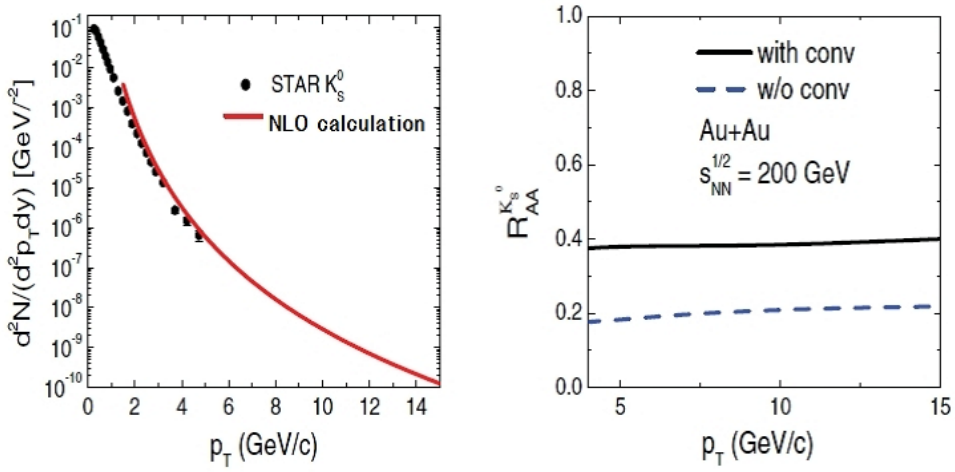

Figure 1.5: K0s spectra from quark and gluon jet fragmentation in p+p collisions at $\sqrt{s_{NN}} = 200GeV$[8]. Data are from STAR Collaboration[9]. R_{AA} for $K^0{}_S$ in $Au + Au$ collisions at same center mass energy as a function of transverse momentum [11].

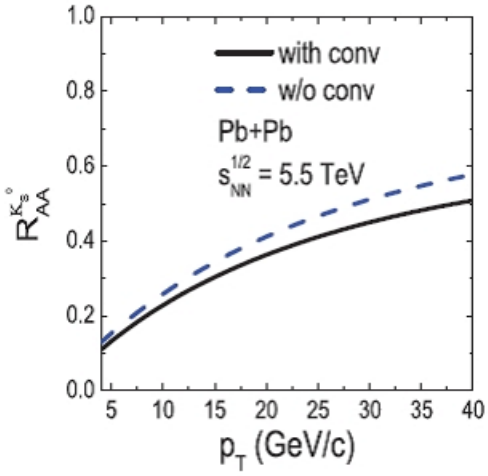

Figure 1.6: R_{AA} for $K^0{}_S$ in $Pb+Pb$ collisions at $\sqrt{s_{NN}} = 5.5TeV$ as function of transverse momentum[11].

Chapter 2

Experimental setup

2.1 The RHIC accelerator

The Relativistic Heavy Ion Collider(RHIC) was proposed in 1990 initially and built in the Brookhaven National Laboratory(BNL) in the United State of America. Simply stated the RHIC is a colliding-beam accelerator which has two ring synchrotrons. The RHIC has provided collisions of various ions, that is proton, deutron, Cu and Au, for about ten years. The designed luminosity is $2 \times 10^{26} cm^{-2} s^{-1}$ for Au + Au and $2 \times 10^{32} cm^{-2} s^{-1}$ for p + p. The bunch crossing intervals is 106 nsec when there are 120 bunches in each ring.

The RHIC is designed to accelerated protons up to 250 GeV and Au nuclei up to 100 GeV per nucleon. I state about the Au ion beam, its journey starts in the Tandem Van de Graaff and accelerated up to 1 MeV per nucleon. The Tandem Van de Graaff consists of two electrostatic accelerators which is capable of producing voltage up to 15 million volts, and the ions are injected into the Booster. The Booster accelerates them up 95 MeV per nucleon. They are injected into the Alternating Gradient Synchrotron (AGS) and accelerated to 8.86 GeV. When the ion beam reaches top speed in the AGS, they are injected into the next beamline called the AGS-To-RHIC (ATR) transfer line.

The RHIC's 3.86 km ring has six intersection points where its two rings of accelerating magnets cross, allowing the particle beams to collide. At these intersection points, four current experiments can operate, these are STAR, PHENIX, PHOBOS and BREAMS.

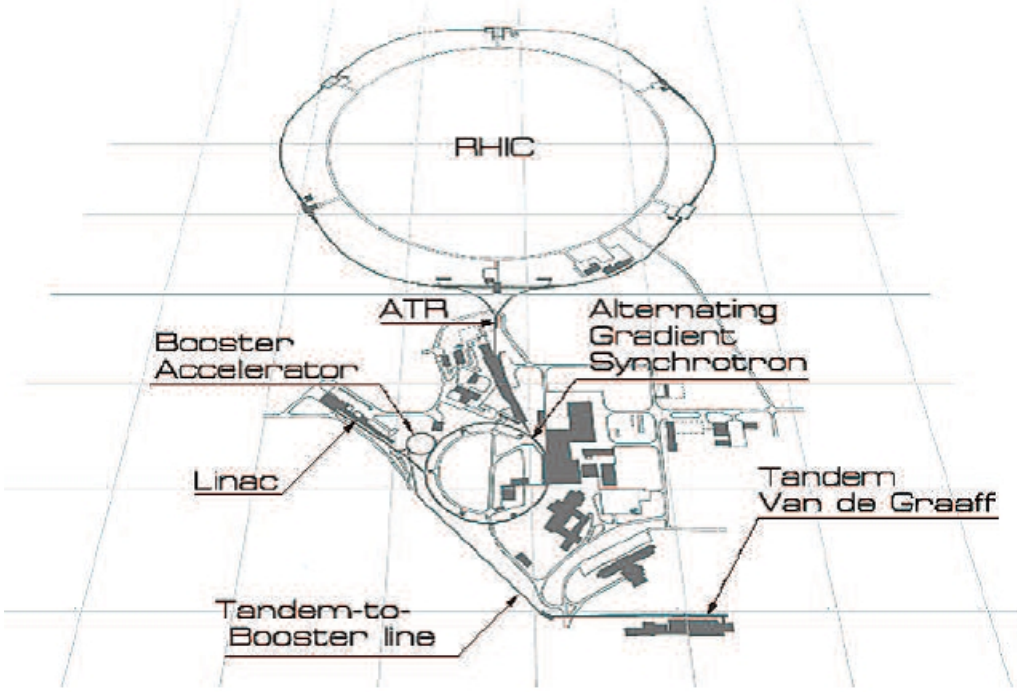

Figure 2.1: Schematic view of the RHIC complex[16].

PHENIX, the Pioneering High Energy Nuclear Interaction eXperiment, is the largest of the four experiments. PHENIX is designed specifically to measure direct probes of the collisions such as electrons, muons, and photons by its multi purpose detectors. In the subsequent sections we describe the PHENIX detector and its various detector components.

2.2 The PHENIX detectors

2.2.1 PHENIX complex overview

In the following a short survey of PHENIX experiment[6] will be given. As the focus of this work is the search for long-lived netural K mesons with ElectroMagnetic Calorimeter(EMCal), decribing them in more detail in 2.2.4.

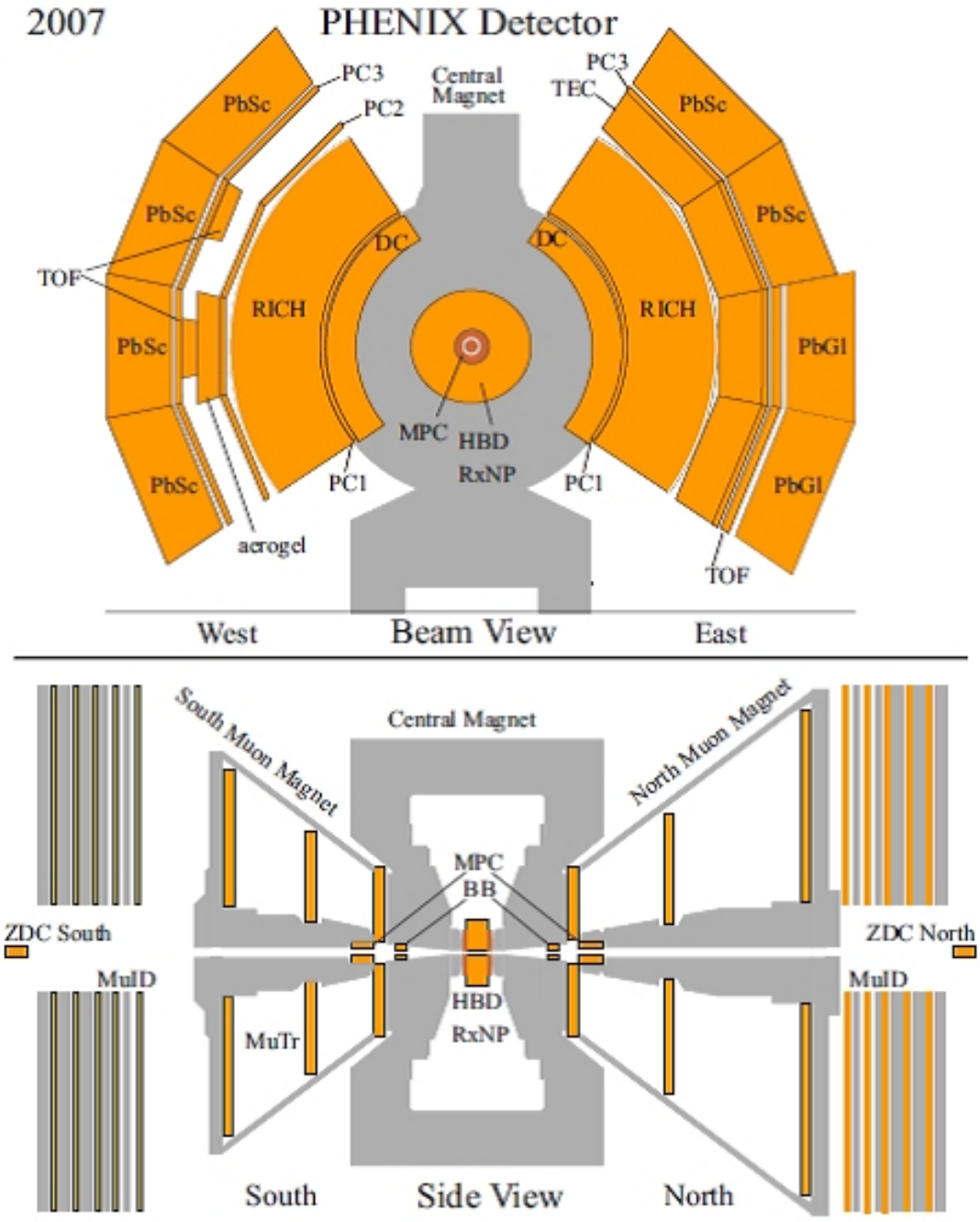

Figure 2.2: The PHENIX Detector configuration(2007)[17].

2.2.2 Zero Degree Calorimeter(ZDC)

Simply stated the ZDCs consist of two hadron calorimeters located at $\pm 18.25m$ from the primary vertex between deflecting dipole magnets of RHIC magnet system. The ZDC design goals are three. First is to provide a common luminosity measurement for all RHIC experimetns. In fact, the ZDC are positioned at each offour RHIC experiments. Second is to provide a common centrality determination with the BBC(below stated). Third is to provide a minimum bias trigger free of beam gas background.

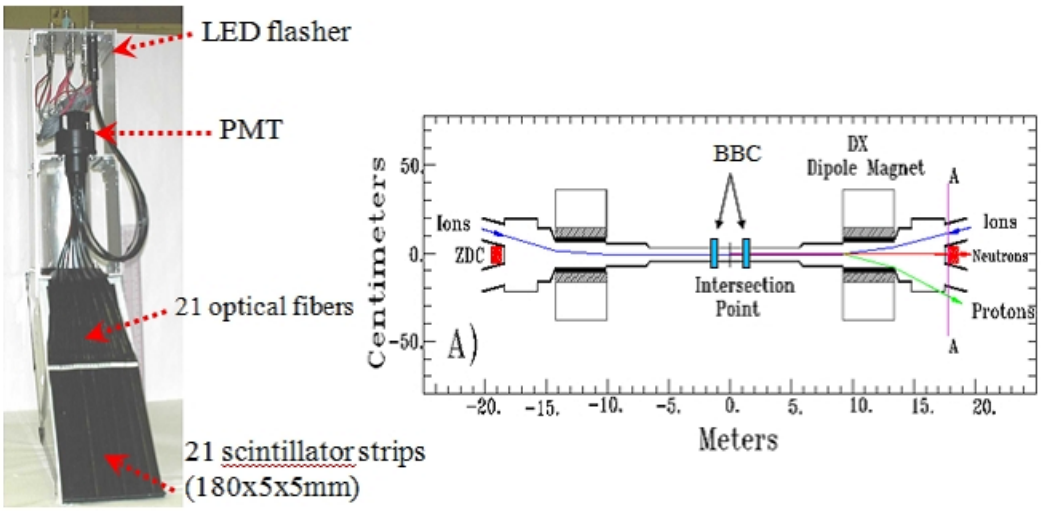

Figure 2.3: The configuration and the location of Zero Degree Calorimeter(ZDC)[18].

North and south ZDC is made of alternating tiles of plates of tungsten and layers of optical fibers. The direction of the plates and layers are tilted by 45 degree relative to the incident neutron direction. The ZDC is designed to measure the number of neutron from the collision to collect the Cerenkov light. A high energy neutrons from the collision generate some perticles, pions, protons and neutrons etc, to interact with nucleus of the tungsten absorber. Generated particles make same interactions again and again, we measure the Cherenkov light from the generated charged particles.

2.2.3 Beam Beam Counter(BBC)

The BBC is hexagonal quartz Cherenkov radiator installed on about one and a half meters from the center of PHENIX detector for both North and South arm along beam axis. The design purposes of the BBC are five. First is to provide a collision vertex. Second is to provide a common centrality determination with the ZDC. Third is to provide a minimum bias trigger. Fourth is to provide a time-zero determination. Fifth is to provide a reaction plane determinaion.

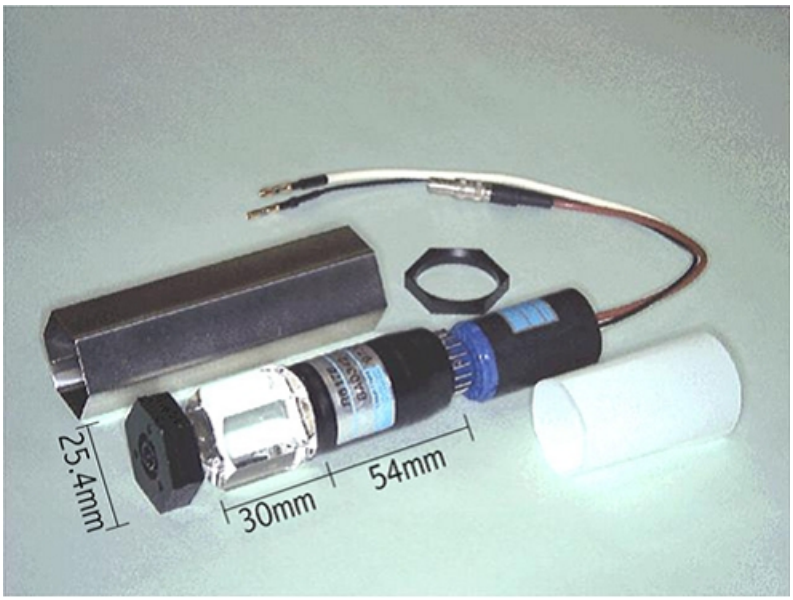

Figure 2.4: One element of Beam Beam Counter(BBC)[19].

I said, The BBC element is a quartz Cherenkov raditor. we can measure a multiplicity of charged particles having $\beta > 0.7$ in the forward rapidity range, here β is a ratio of velocity of charged particle and velocity of light(c). Each photon-multiplier converts cherenkov light into electrons in order to measure it as electrical signals.

The BBC consists of two identical sets of counters installed on both sides of the collision point along the beam axis. One set is comprised of 64 BBC elements. The interaction position along the beam axis is calculated from individual time measurements of fast leading particles hitting BBC elements

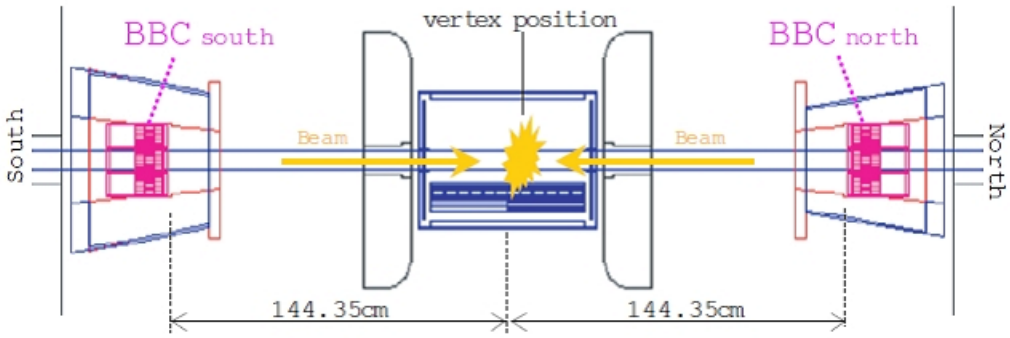

Figure 2.5: The location of Beam Beam Counters north and south(BBC)[19].

on the both sides of the interaction point. With an intrinsic timing resolution of 70 ps, BBC determines the interaction position with a precision of 0.6 cm.

2.2.4 Electro-Magnetic Calorimeter(EMCal)

The EMCal of PHENIX is an electro-magnetic calorimeter at mid rapidity. The calorimeter measures position, energy and time of flight of incoming particles. Basically the principles of detection is that electrons and photons interact electromagnetically, bremsstrahlung and pair production, and produce electromagnetic showers. In the case of hadrons, these particles in this energy range are typically Minimum Ionizing Particles(MIPs) and deposit only part of their energy in hadronic showers. This EMCal of PHENIX has two parts, sampling calorimeter(PbSc) and homogeneous, leading-glass volume cherenkov radiator(PbGl).

Lead Scintillator Calorimeter (PbSc)

The PbSc electromagnetic calorimeter is a sampling calorimeter made of alternating tiles of Pb ans scintillator consisting of 15552 individual towers and covering an area of approximately $48m^2$. The PbSc module consists of four towers, each with 66 layers of 0.15 cm lead abosorber and 0.4 cm scintillator. The layers are optically connected via wavelength-shifting fibers for light collection by a photon-multiplier. Groups of 6×6 modules are connected mechanically to a self-supporting supermodule, with 3×6 PbSc

supermodules forming one sector. One mechanical supermodule contains 144 towers and is read out by one Front-End-Module(FEM).

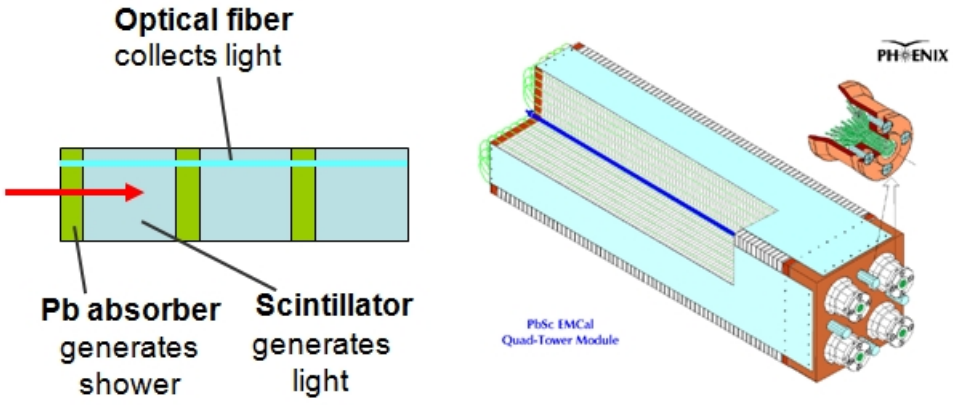

Figure 2.6: (left)Interior view of one PbSc tower, consisting of 66 layers, this show only 3 layers (right)Interior view of one PbSc module, consisting of four towers[20].

The Front-End-Modules differ in detail for various subsystems but their general layout is similar. They consist of the Front-End-Electronic(FEE), which digitalizes the analog signals from the detector elements and buffer the data to wait for trigger decisions.

Lead Glass Calorimeter (PbGl)

The PbGl has two sector and each lead-glass sector consists of 192 supermodules. One supermodule is formed by an array of 6×4 lead-glass modules, each with a size of $4 \times 4 times 40 cm^3$ and wrapped in reflecting mylar foil and shrink tube. Each lead-glass module is read out via a photon-multiplier.

The lead-glass calorimeter(PbGl) is a cherenkov calorimeter(n = 1.647). For example, high energetic photons incident on the PbGl interact mainly via electron-positron pair production and the produced electrons and positrons subsequently lose their energy by radiating Bremasstrahlung. These photons can again produce electron and positron pairs, resulting in the formation of an electromagnetic shower. Of course there are other processes such photo-

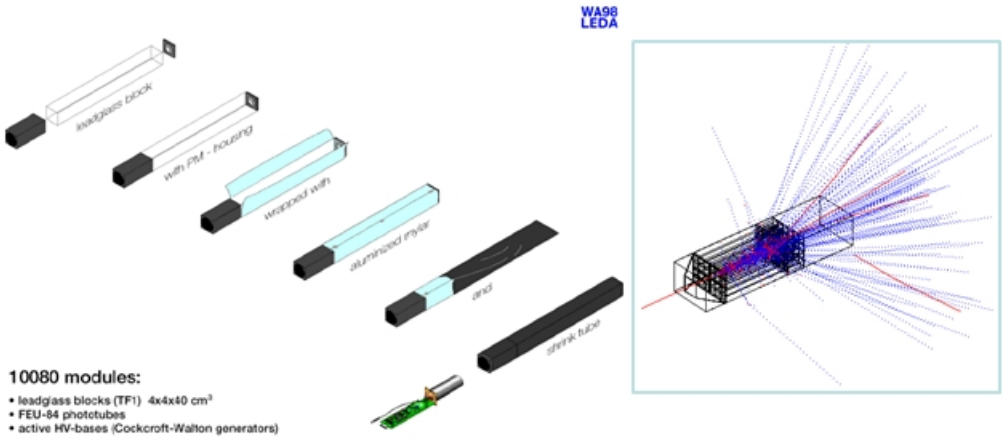

Figure 2.7: A PbGl tower and image of one supermodule[20].

electronic effect and Compton scattering. But they play only minor role in this energy range.

In the case of hadrons, such as pions and protons, form a so-called hadronic shower. Its charactreistic quantity is the nuclear interaction length, the distance where most of the hadrons suffer an inelastic interaction and form further hadrons, mostly pions. Charged hadrons are called Minimum Ionizing Particles(MIPs). Their energy loss is given by the Bethe-Bloch equation. It is constant over a wide energy range leading to the formation of characteristic MIP peak.

cluster Algorithm

The EMCal readout electronics comprisesalmost 25000 readout channels. For both EMCals 144 individual towers are read out by one single FEM.

An electromagnetic shower usually spreads over more than one tower, all towers are calibrated by the Cluster Algorithm I state below.

The towers with more than a threshold are selected. For the cluster merging, the effect of fusion of a "true" cluster and a "background" cluster, selected cluster is defined by assuming that they are all photons, an isolated cluster is split into two clusters in the way that the number of clusters is equal to the number of local maximum in the isolated cluster. In the other word,

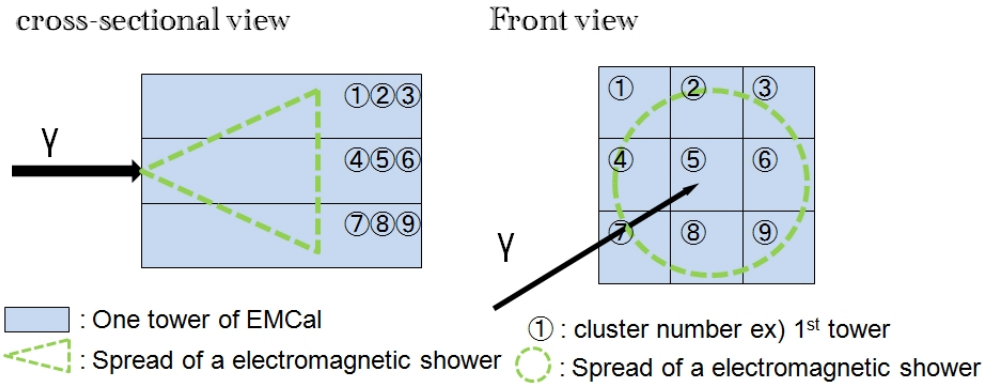

Figure 2.8: Image of a cluster.

if more than one local maximum is found, we split this cluster according to amplitude and positions of the local maximum.

In a simple case that single photon hit in middle of a EMCal tower like a figure2.8, the E_{core}, energy of the "core" towers, is defined as;

$$E_{core} = \sum_{i}^{core} E_i^{means}, \tag{2.1}$$

where E_i^{means} is the measured energy in i-th tower and $\sum_i^{core}$ is defined as summing of the towers(1st, 2nd, 3rd, 4th, 6th, 7th, 8th and 9th towers) belonging to the "core" towers(5th tower). We demand that the "core" towers are in the following condition,

$$\begin{aligned} \frac{E_i^{pred}}{E_{all}^{mean}} &> 0.02, \\ E_{all}^{mean} &= \sum_{i}^{all} E_i^{mean}, \end{aligned}$$

where E_{all}^{mean} is the sum of measured energy in all towers belonging to the "peak-area"(1st to 9th), E_i^{pred} is the predicted energy using shower profile in i-th tower. The averaged number of towers belonging to the "core" towers is 4 towers(2nd, 4th, 6th and 8th).

In fact the E_{core} contains 91.8 percents energy of total energy on average. The energy fraction of the E_{core} to the total energy depend on the incident

angle, position and energy. The dependence is studied by the GEANT simulation tuned by using obtained performance in test beam and corrected in the data analysis.

2.2.5 Data acquisition system(DAQ)

The RHIC provide the high interaction rates of approximately 500kHz in $p+p$ collisions and the large event sizes in high multiplicity $Au+Au$ events at a rate of a few kHz. However the bunch crossings occur at a frequency of 9.43 MHz. This means events have a minimum timing distance of about 106 nano second[ns]. In PHENIX the timing signal is distributed by the Master Timing System(MTS) to all FEM's which participate in the data collection process.

PHENIX Timing System

The RHIC clock is provided by the Accelerator Control(AC) group. This key signal is sent via optical serial links to the Master Timing Module(MTM), the first stage of the PHENIX timing system. The MTM sends a copy of the RHIC clock to the Granule Timing Modules(GTM's) and local level one(LVL1) trigger system. PHENIX detector system is divided into two sets of elements: granules and partitions. The GTM's are synchronized by the MTM. They manage busy signals from DCM's, relay them to the LVL1 trigger system and provide the RHIC clock and LVL1 trigger accepts to the granules, it means FEM's.

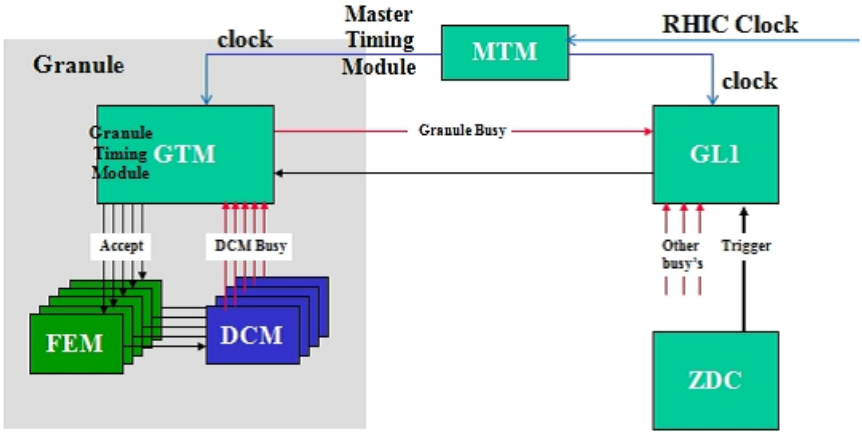

Figure 2.9: Block diagram of the PHENIX Online System[21].

Chapter 3

Analysis

3.1 Analysis Method

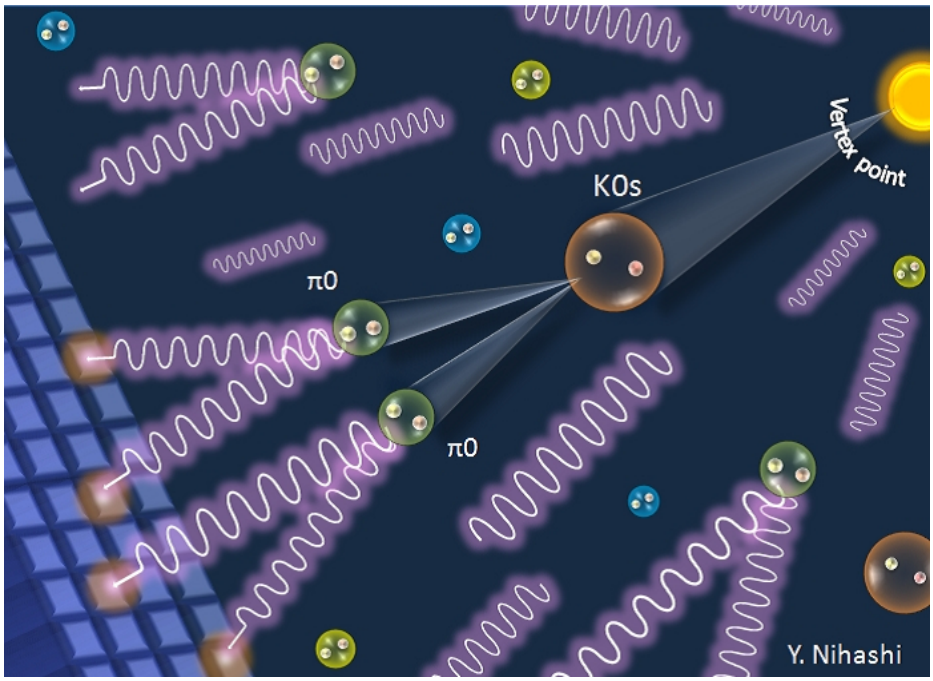

Figure 3.1: Image of the 2 π^0 decay mode of ${K^0}_S$ hitting to the EMCal. ${K^0}_S$ decay into 2 π^0 and each π^0 decay into 2 γ.

This basic idea of the identification of short-lived neutral K meson(${K^0}_S$) is rather simple: Basically we can measure only the energy and the position of FINAL-STATE particles depending on detectors. So we reconstruct the particles info before decay with final-states' energy, in the case of neutral π meson(π^0) we reconstruct π^0s from photon(γ) pairs; 98.8 % of π^0 is going to 2 γ. For the identification of the parent-particle we calculate the invariant mass, a Lorentz invariant value of four-momentum. Therefore the invarinat mass of π^0 is,

$$ {M^2}_{\pi^0} = 2E_1E_2(1 - \cos\theta_{\gamma_1\gamma_2}), \tag{3.1} $$

where E_1 and E_2 are the measured energy of each γ (suppose γ_1 and γ_2 arbitrarily) and $\theta_{\gamma_1\gamma_2}$ is the opening angle between γ_1 and γ_2 calculated from hit positions.

It is known that almost ${K^0}_S$ decay into π mesons; 69.20 % of ${K^0}_S$ is going to π^+ and π^-, 30.69 % of ${K^0}_S$ is doing to 2 π^0. Basically we measure the momentum of charged particles with their flight in a strong magnetic field. hence we can't measure the momentum of high energetic particles naively.

The measurement of ${K^0}_S$ via 2 π^0 decay mode is very challenging, because of the lage combinatorial background in the heavy ion collisions. The combinatorial background of ${K^0}_S$ via 2 π^0 ,${}_nC_4$, is about the square-fold of the number of clusters(photons) as large as it of π^0.

First we reconstruct π^0 pair from γs and select ${\pi^0}_1$ and ${\pi^0}_2$ as ${K^0}_S$-origin candidates. I measure the two gamma invariant mass peak from π^0 and I confine to two gamma invariant mass value with a gaussian fitting.

$$ {M^2}_{{\pi^0}_1{\pi^0}_2} = (E_1 + E_2 + E_3 + E_4)^2 - ({p_x}^2 + {p_y}^2 + {p_z}^2), \tag{3.2} $$

where

$$ \begin{aligned} p_x &= \frac{x_1E_1}{\sqrt{{x_1}^2 + {y_1}^2 + {z_1}^2}} + \frac{x_2E_2}{\sqrt{{x_2}^2 + {y_2}^2 + {z_2}^2}} \\ &+ \frac{x_3E_3}{\sqrt{{x_3}^2 + {y_3}^2 + {z_3}^2}} + \frac{x_4E_4}{\sqrt{{x_4}^2 + {y_4}^2 + {z_4}^2}} \\ p_y &= \frac{y_1E_1}{\sqrt{{x_1}^2 + {y_1}^2 + {z_1}^2}} + \frac{y_2E_2}{\sqrt{{x_2}^2 + {y_2}^2 + {z_2}^2}} \\ &+ \frac{y_3E_3}{\sqrt{{x_3}^2 + {y_3}^2 + {z_3}^2}} + \frac{y_4E_4}{\sqrt{{x_4}^2 + {y_4}^2 + {z_4}^2}} \end{aligned} $$

$$p_z = \frac{z_1 E_1}{\sqrt{{x_1}^2 + {y_1}^2 + {z_1}^2}} + \frac{z_2 E_2}{\sqrt{{x_2}^2 + {y_2}^2 + {z_2}^2}} + \frac{z_3 E_3}{\sqrt{{x_3}^2 + {y_3}^2 + {z_3}^2}} + \frac{z_4 E_4}{\sqrt{{x_4}^2 + {y_4}^2 + {z_4}^2}}$$

(the coordinates of x, y and z are defined in the Appendix).

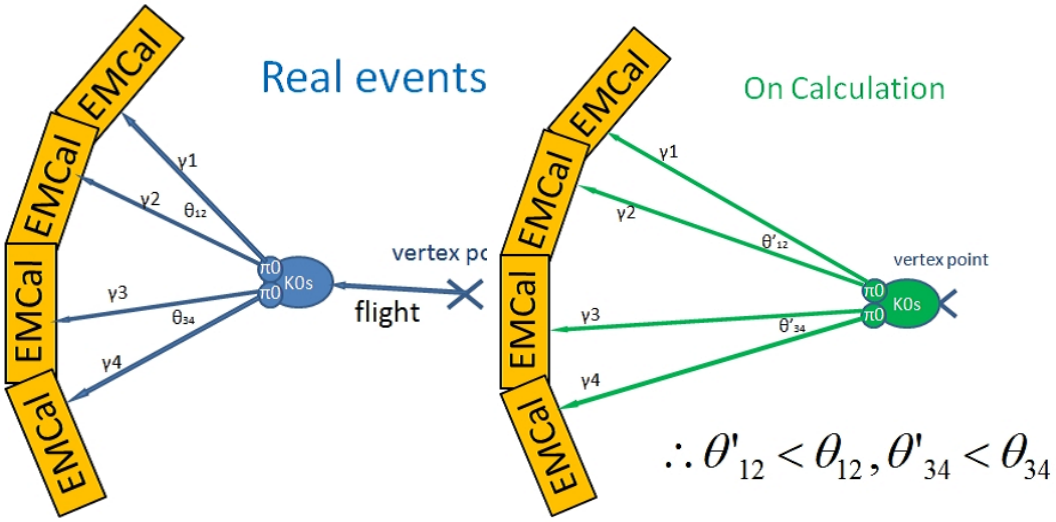

Figure 3.2: Schematic view of a single $K^0{}_S$ event in the real event, here θ_{12} is the true opening angle between γ_1 and γ_2, and θ_{34} is the true opening angle between γ_2 and γ_4

Figure 3.3: Schematic view of a single K^0_s event on calculation, here $\theta'{}_{12}$ is the calculated opening angle between γ_1 and γ_2, and $\theta'{}_{34}$ is the calculated opening angle between γ_2 and γ_4

With these calculations we can see the $K^0{}_S$ signals as the peak in the four-gamma invariant mass distribution. However the mean life time of $K^0{}_S$ is realtively long, these signals may change. In reality, $K^0{}_S$s' mean life($\tau_{K^0_s}$) is $0.8958 \pm 0.005 \times 10^{-10}$ second [12]. It is so long comparatuvely that the high energetic $K^0{}_S$ (velocity $\sim$ light speed(c)) can fly according to the his life time and his momentum. I anticipate that some mass shifts "only on above calculattion" will arise as a result of this life time effect (see figure3.2,3.3). In

other words, it may change the signal shape and the peak positions. The basic reason is that we can't measure the particles flight near the vertex position until setting new detector. We calculate the invariant mass assuming ${K^0}_s$ decay at the vertex position. Hence we miscalculate the opening angles of π^0s from ${K^0}_S$, the value of π^0 invarinat mass and ${K^0}_S$ invariant mass look smaller than each vacuum mass (See figure3.2 and figure3.3).

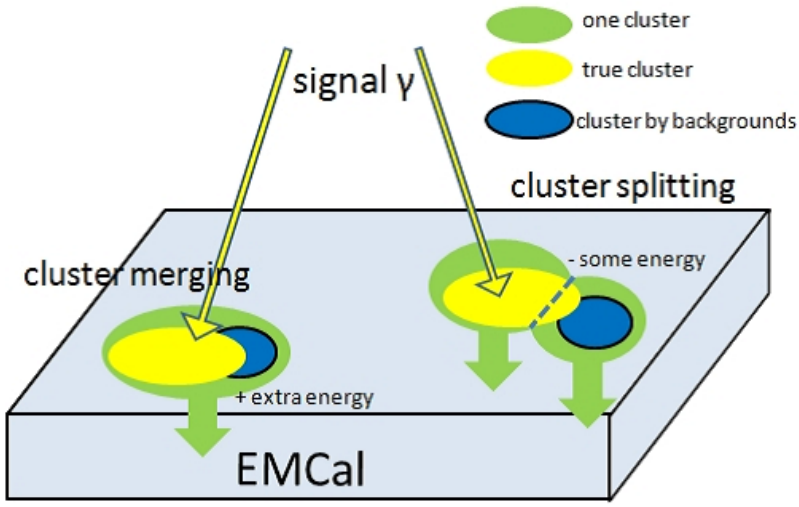

Figure 3.4: Diagram of the cluster merging and the cluster spliting on a cluster algorithm.

In addition, we have to take it into account the multiplicity dependence as long as dealing with collisions of a high particle multiplicity such as Au + Au collisions at $\sqrt{s_{NN}}$ = 200 GeV. Since the matrial for this analysis is photon(γ), so we discuss only the ErectroMagnetic Calorimeter detects photons at PHENIX. To tell the truth, this multiplcity generates huge background and naturally those backgrounds interfere a cluster algorithm. We consider two effects, the one is the cluster merging and the other is the cluster splitting (See figure 3.4). The former is the effect of integration of a "true" cluster and a "background" cluster, here "true" cluster means a cluster generated by only a photon from ${K^0}_S$. Because of high particle multiplicity there are many clusters generated by another hadrons around a true cluster. Then

we may measure the energy merged with the deposited energy from another hadrons. To put it another way, it is probably true that we may detect larger energy than the energy deposited only by a signal γ. The latter is the effect of separation of a "true" cluster. Because of high particle multiplicity we may measure the energy of another hadrons merged with a piece of a true cluster. Finally, we may detect smaller energy than the energy deposited only by a signal γ.

I estimate these effects with the simulation quantitatively. In the next section, I describe the simulation method and its results in detail.

3.2 Single simulations

Simulation method is a effective way to estimate measured results quantitatively with a large statistics. Generally speaking, what they have several stages results from the fact that there is several stages in heavy-ion collisions. It is different which processes we reconstruct. Briefly, there are four processes in the simulation we used. First is the simulation of collisions. The two ion beams accelerated by RHIC will collide and interact. With enough statistics the yields of generated particles go along each cross section measured or expected. Second is the simulation of generated particles from vertex, it means a One's outputs. Third is the simulation of detector response in particles flying, it means two's outputs are three's inputs. Fourth is the simulation to change the simulated-data ,third outputs, into the offline Summary Tables(DST). , where the raw data are converted into quantities with more physical meaning. In this thesis work I simulate second, third and fourth processes.

3.2.1 Event Generator

We used the one of event generators called as "EXODUS"[13] based on Monte Carlo codes. I used it to generate the input single particles. For purposes of this simulation program, an event is viewed as a list of the particles with their type, energies, momenta, the point of peroduction and the time of production. We can let off ${K^0}_S$ having these status as I do. For instance, we let off ${K^0}_S$ having full range in order to estimate a geomertrical acceptance for ${K^0}_S$. Then we can't gain the yield of low p_T ${K^0}_S$ enough, we change the input particle p_T distribution to it enhanced at low p_T.

- $4 \leq p_{T\,{K^0}_S} \leq 14[GeV]$, p_T distribtion is flat in a figure3.5,
- $-0.5 \leq$ y(rapidity) ≤ 0.5, rapidity distribtion is flat,
- $0 \leq \phi < 2\pi$, ϕ distribution is flat,
- Branch ratio of ${K^0}_S$ to 2 π^0 is 30.69 percents,

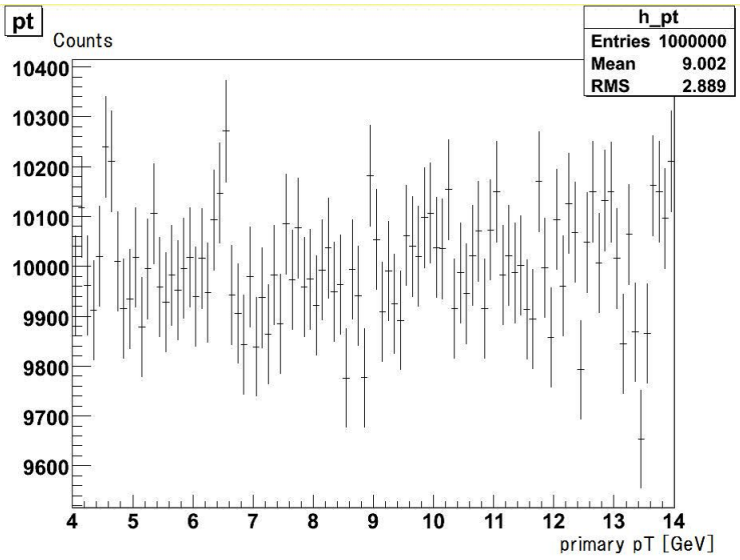

Figure 3.5: The p_T distribution of primary ${K^0}_S$.

3.2.2 Detector Simulation

As you see the figure2.2, the PHENIX detectors are so complex divided their resposibilities. There are a large of detector types and matrials inside it. The PHENIX Integrates Simulation Application(PISA) is introduced in order to simulate all response in the PHENIX complex. PISA is the PHENIX simulation software package based on GEANT libraries [14]. Using PISA, a PHENIX simulator can recognize aspects of the whole PHENIX detectors' geometry and materals and convert the GEANT particle tracking into simulated detector signals.

When I measure photon energy with PbSc EMCal, charged π meason is expected as a huge background. High energetic cahrged particles lose energy in matter. With respect to PbSc EMCal, there is 66 layers of 0.15 cm lead abosorber. In brief, charged particles go through 9.9 cm lead abosorber at least. At RHIC energy, most relativistic particles have mean energy loss rates close to the minimum, and are said to be minimum ioninzing particles(MIPs). I'll take the case of $-\frac{dE}{dx} = 2[MeVg^{-1}cm^2]$[12], charged π meason lose energy about 225 MeV. To tell the truth, charged particles do not go straight in the lead due to multi-scattering. I use clusters having more than 300 MeV energy as hard cut in order to rid all cluster of clusters from charged π mesons.

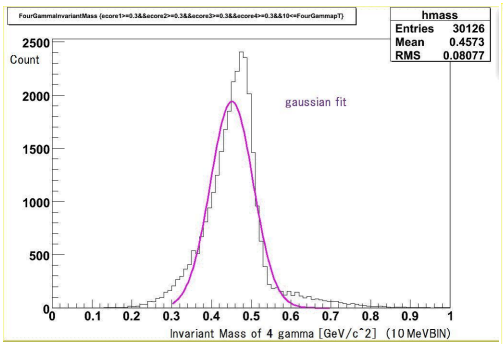

Figure 3.6: Invariant mass spectrum of single $K^0{}_S$ events for high p_T with a gaussian fitting.

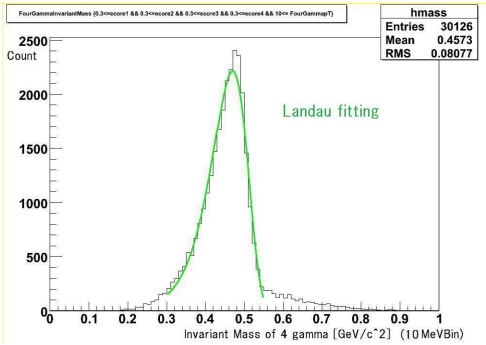

Figure 3.7: Invariant mass spectrum of single $K^0{}_S$ events for high p_T with a landau fitting.

As you see the figure3.6, Once I use the gaussian as a fitting function, a distribution of 4 photons invariant mass looks asymmetry due to the life time effect.

Then, I try to fit this four photons invariant mass distribution with the modified landau function (See the figure3.7). Here,

$$\text{landau function} \equiv f(x) \equiv A \times \exp[\frac{x-C}{B} - \exp(\frac{x-C}{B})], \tag{3.3}$$

$$\text{gaussian function} \equiv g(x) \equiv \frac{1}{D\sqrt{2\pi}} \exp(\frac{-(x-E)^2}{2D^2}), \tag{3.4}$$

where A, B, C, D and E are the fitting parameters. I define that B is a width and C is the most probable value for landau function, D is a width and E is mean value for gaussian function.

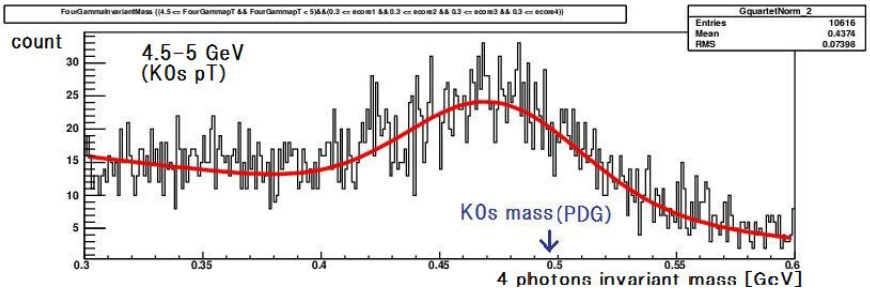

Figure 3.8: four gamma invariant mass distribution in 4.5GeV $\leq {p_T}^{K^0 S} \leq$ 5GeV with a gaussian fit.

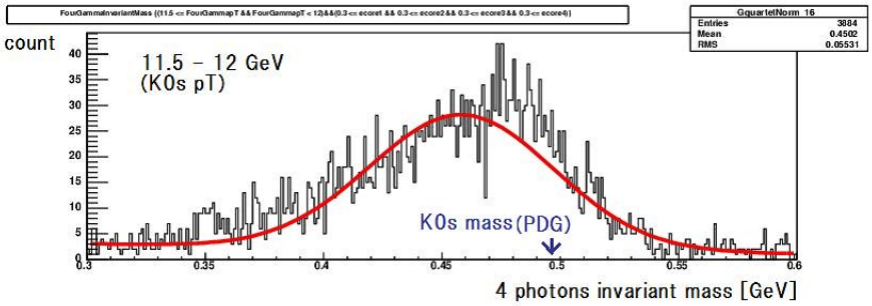

Figure 3.9: four photons invariant mass distribution in 11.5GeV $\leq {p_T}^{K^0 S} \leq$ 12GeV with a gaussian fit.

I show the figure3.8 and the figure3.9. I separate the four photons invariant mass spectra according to four photons p_T, one p_T bin range is 0.5GeV,

than one bin in the figure3.6, 10 GeV $\leq p_T \leq$ 14 GeV. I fit these distributions with a gaussian and a linear function. There is a enhaced counts around 0.5 GeV in the figure3.9 and the figure3.8 don't look so.

Here, we have to take into consideration that the ${K^0}_S$ life time is relatively long and we can't measure the track very near collision vertex. As I stated the life time effect in the previous section, this effect lead to like a lower mass shift in invarant mass distribution. In this respect, it is expected that the mass peak is changing according to the ${K^0}_S$ p_T. So there are flater distribution in the wide p_T range like the figure3.6. I suggest a way to modify this effect in next section.

3.2.3 Comparison between the landau fitting and gaussian fitting for 4 photons invariant mass distribution

I stated that the langau fitting looks fine more than the gaussian fitting for 4 photons invariantmass distribution. I show the results of the comparison between the landau fitting and gaussian fitting in the figure3.10, the figure3.11 and the figure3.12. There is easily no comparison between gaussian mass peak and landau peak due to these function characteristics. Gaussian peak means a mean of invariant mass value of a peak, meanwhile landau peak means a most probable invariant mass value of a peak. In a figure**??**, for all p_T range(7-14 GeV) landau peak values are larger than gaussian peak values and both values are smaller than a vacuum mass of ${K^0}_S$; 0.498 GeV.

In a figure3.12 for all p_T range landau fitting converted χ^2s are smaller than gaussian fitting converted χ^2s. It means a landau fitting looks fine more than a gaussian fitting. So I use a landau fittig for 4 photons invariant mass distribution.

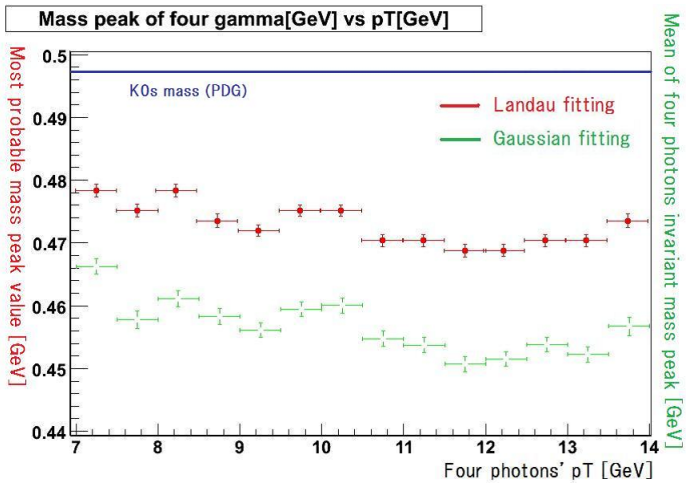

Figure 3.10: Peak position of the $K^0{}_S$ as a function of the p_T with the landau and gaussian fitting.

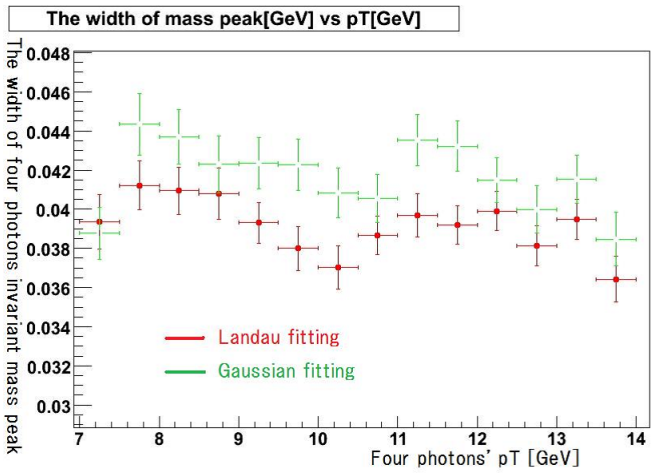

Figure 3.11: Peak width of the $K^0{}_S$ as a function of the p_T with the landau and gaussian fitting.

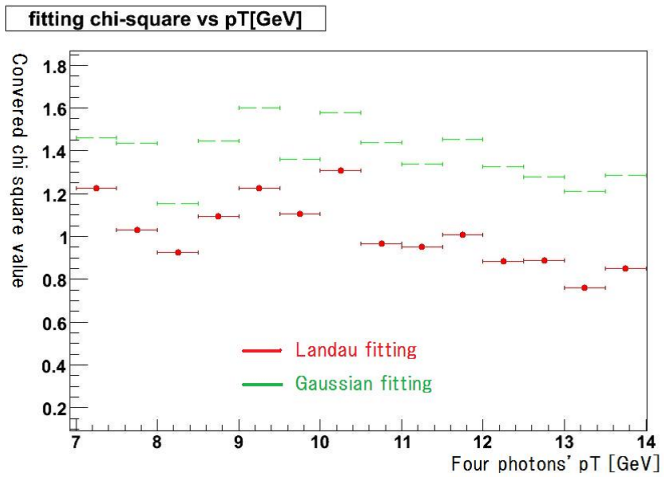

Figure 3.12: Chi square of the landau and gaussian fitting about the mass peak of the ${K^0}_S$.

3.2.4 Estimation of the Decay Vertex Location

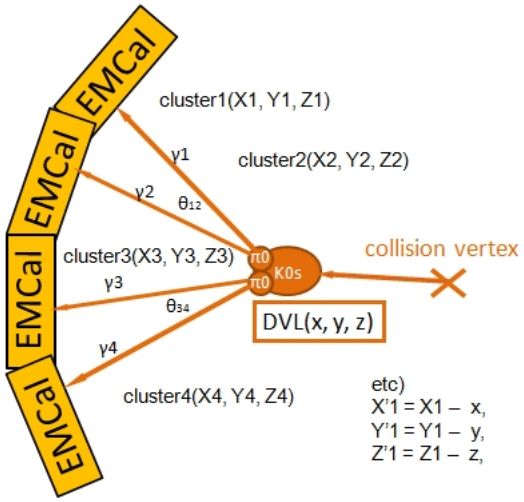

Figure 3.13: Image of Decay Vertex Location(DVL).

In the previous section, we stated the life time effect. It is difficult to measure each ${K^0}_S$ lifetime, it is possible to reconstruct a ${K^0}_S$ and measure each ${K^0}_S$ momentum with the EMCal. In addition it is known that the mean life time of ${K^0}_S$ is 0.8953×10^{-10} second.

I fix that all ${K^0}_S$ life time is the mean life time. Then I calculate the most probable Decay Vertex Location(DVL). The mean life time is the time until a ${K^0}_S$ decay in the ${K^0}_S$ rest frame. High energetic ${K^0}_S$ travels at almost the speed of light. For an observer on the earth(labratory system) the rapidly moving reference frame of ${K^0}_S$s elapse more slowly, the ${K^0}_S$ mean life time is lengthened to $\gamma\ \tau_{{K^0}_S}$.

$$DVL_{x,y,z}[m] = v_{{K^0}_S} \times \gamma \times \tau_{{K^0}_S} \frac{P^{{K^0}_S}\vec{}_{x,y,z} c}{\mid P\vec{K^0}_S \mid c} \tag{3.5}$$

$$= \frac{P^{{K^0}_S} c}{E_{{K^0}_S}} \times c \times \frac{E_{{K^0}_S}}{M_{{K^0}_S} c^2} \times \tau_{{K^0}_S} \frac{P\vec{K^0}_S{}_{x,y,z} c}{\mid P\vec{K^0}_S \mid c} \tag{3.6}$$

$$= \frac{c \times \tau_{{K^0}_S}}{M_{{K^0}_S} c^2} \times c P^{{K^0}_S}\vec{}_{x,y,z} \tag{3.7}$$

$$\sim \quad 0.053941408 \times cP^{\vec{K^0{}_S}}{}_{x,y,z} \tag{3.8}$$

where c is the speed of light [m/s], $\tau_{K^0{}_S}$ is 0.8953×10^{-10}[s], $M_{K^0{}_S}c^2$ is 0.497614 $[GeV]$ and $\mid P^{\vec{K^0{}_S}} \mid c$ is a calculated probablely momentum [GeV] of a reconstructed $K^0{}_S$. For instance, a calculated probablely momentum is 14 GeV, then $K^0{}_S$ is alive for 0.76 m from a collision vertex.

I recalculte the vectors of clusters from the DVL. Naively this recalculation is expected to modify the π^0 opening angle, the calculated invarinat mass of π^0 and the calculated invariant mass of $K^0{}_S$.

The comparison between the DVL analysis and the normal analysis

I report the comparison between the Decay vertex location(DVL) analysis and the "normal" analysis here. The main difference between the former and the latter is whether I recalculate the invariant mass of four photons with the most probable decay vertex location or not.

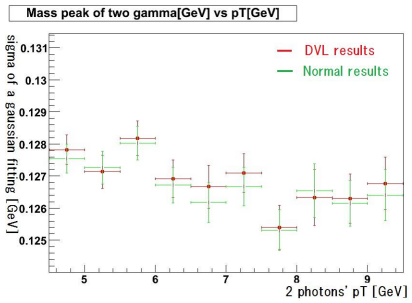

Figure 3.14: Invariant mass peak of 2 photons with gaussian fitting. The red line is to take into account the DVL. The green line is not to take into account the DVL.

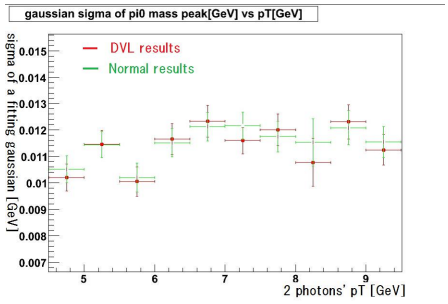

Figure 3.15: The width of the 2 photons invariant mass with gaussian fitting. The red line is to take into account the DVL. The green line is not to take into account the DVL.

I fit the constant in a figure3.14 and a figure3.15 to get cut-values when I calculate the four photons invariant mass and to reduce backgrounds. These results are shown in a table3.1;

Table 3.1: The results of the fitting of the peak position and the width in two photons invariant mass distribution.

	most probable mass value [GeV]	width of the mass peak [GeV]
DVL results	0.127073	0.0113321
Single results	0.126865	0.0114572

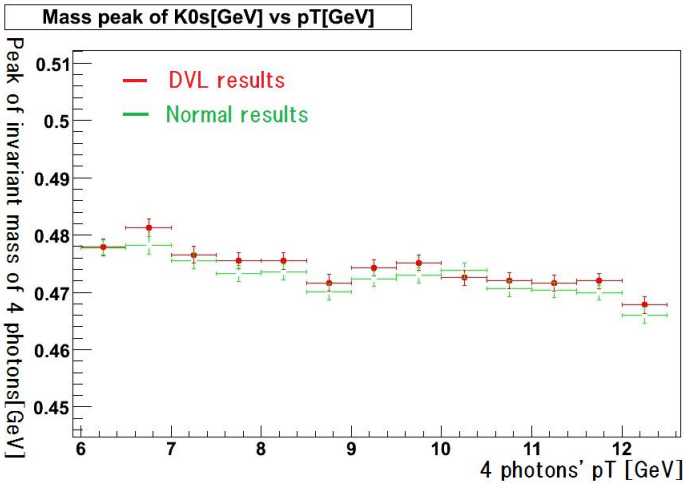

Figure 3.16: Peak of the 4 photons invariant mass with landau fitting. The red line is to take into account the DVL. The green line is not to take into account the DVL.

A figure3.16 show a most probable invariant mass value of $K^0{}_S$ meason with DVL and without DVL. Each result is separated by color, red plot means DVL results and green plot means normal results, out of consideration of DVL. A figure3.17 show a width of landau fitting in 4 photons invariant mass with DVL and without DVL. A figure3.18 show a χ^2 of each landau fitting.

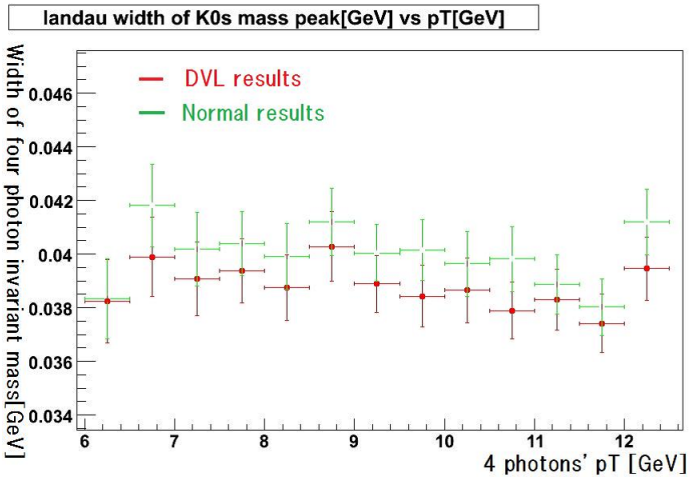

Figure 3.17: Width of the 4 photons invariant mass with landau fitting. The red line is to take into account the DVL. The green line is not to take into account the DVL.

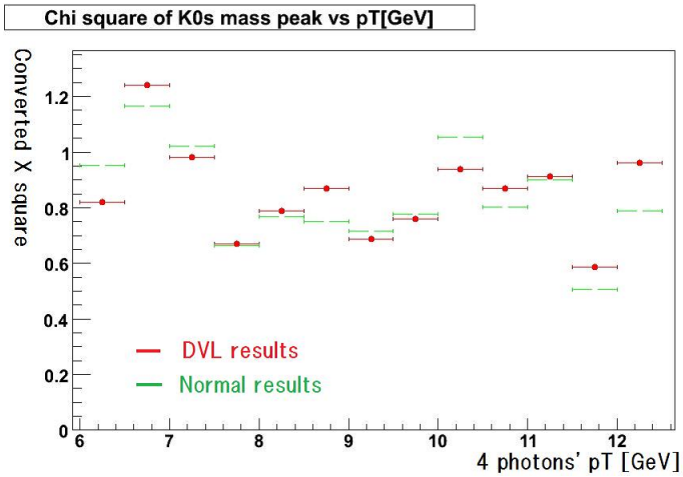

Figure 3.18: χ^2 of a landau fitting. The red line is to take into account the DVL. The green line is not to take into account the DVL.

3.3 Embedding simulation

In the previous section, we stated the mulitiplicity effect. We explain how we take account of the multiplcity effect in this section. We use the technique called "embedding simulation"; embedding of the simulated particles into real event. The main flow of the embedding simulation is described in the following.

For this embedding, a DST(Data Summary Table) containing real data(taken at 2004)is read in together with a few simulated DSTs for single ${K^0}_s$. The simulated events are scaned into devided vertex classes by a z-vertex location and real events are only considered if they satisfy the same collision vertex class. For each selected real event the EMCal tower information, deposited energy, is extracted from the DST and merged with the tower information from one simulated event. The list of merged towers is the basis for a new cluster. For the above-mentioned reason, the result list of merged clusters is different from the list of clusters from the real event. A comparison yields the modified or new clusters in the merged event and the lost clusters from the real event (See Figure3.19).

The embedding output contains also data copied from the real and the simulated DST into new merged DST. This new DST have information such as trigger data of real events and ancerstry information of single ${K^0}_s$ simulation. To sum up, the embedding output have ;

- Such as centrality and vertex, event information from the real event
- Lists of EMCal clusters containing the new hits after embedding,
- Lists of EMCal clusters from the pure single ${K^0}_s$ simulation,
- Simulated particle information, such as parent particles, primary momentum and energy.

I calculate the invariant mass of two photons with this embeded simulation data using the formula3.1. It can be seen that π^0 mesons from ${K^0}_S$ mesons merging to the background.

Energy Asymmetry of cluster pair In contrast to single simulation, there is a huge combinatorial background in embeded simulation. One possibility to reduce background is to apply the energy asymmetry limit; defined as

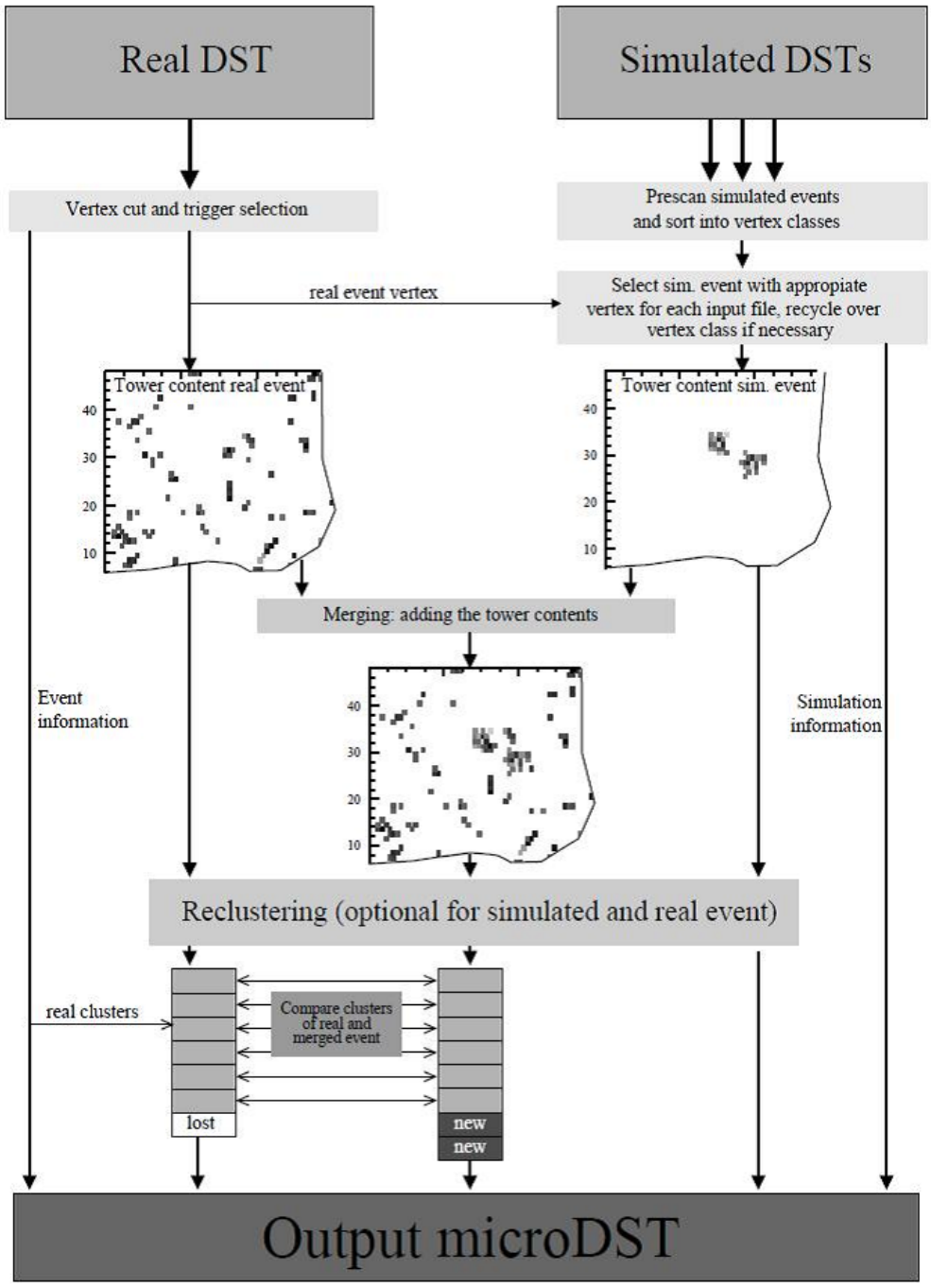

Figure 3.19: Main flow of the embedding algorithm[15].

$$\alpha = \frac{\mid E_1 - E_2 \mid}{E_1 + E_2} \tag{3.9}$$

where E_1 and E_2 is each measured energy. Since a photon pair from π^0 is massless and perfectly symmetric in the π^0 rest frame, a energy asymmetry value is expected 0 in the π^0 rest frame. In the lab system a energy asymmetry distribution from π^0 is flat. On the other hand, a energy of most background is expected relatively low because it is known generically a energy of background has exponential distribution. As a result, a energy asymmetry of background is expected as strongly peaked around 1

2 photons invariant mass spectra After fitting a gaussian function, we get mean and width of a invariant mass of two photons in each centrality bin from these figures like as a figure3.20, a figure3.21, a figure3.22 and a figure3.23. The more it is a central collision, the more the nunmber of generated particles increases. There are larger background in the most central collisions and in minimum bias than in the peripheral collisions. Then, I use a harder energy asymmetry cut, less than 0.7, in order to reduce a combinatiorial background in the most central and in minimum bias. Here, "0-30 percents centrality", "30-60 percents centrality ", "60-92 percents centrality" and "Minimum Bias" mean the high multiplicity, the mid multiplicity, the low multiplcity and no selection of multiplicity respectively in a figure3.23, a figure3.22, a figure3.21 and a figure3.20.

The comparison between embeded simulation and single simulation for the invariant mass distribution of 2 photons

At first I show the embeded and single results of the invariant mass distribution of 2 photons from ${K^0}_S$ in a figure3.24, a figure3.25 and a figure3.26. As a figure3.24, for all p_T range(4-11 GeV), gaussian peak values of embeded simulation are larger than gussian peak values of single simulation. There is no gap of width values between embeded simulation and single simulation in a figure3.25.

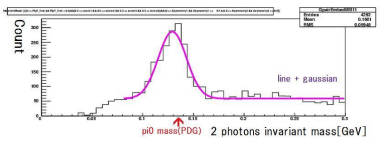

Figure 3.20: The invariant mass of two photons in the range of two photons p_T from 8GeV to 8.5GeV at the Minimum Bias.

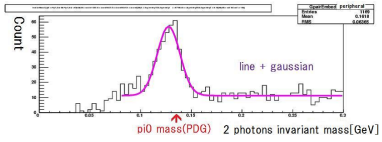

Figure 3.21: The invariant mass of two photons in the range of two photons p_T from 8GeV to 8.5GeV at the peripheral collisions.

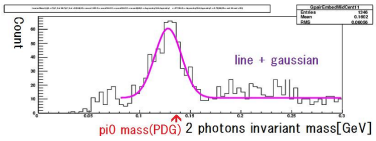

Figure 3.22: The invariant mass of two photons in the range of two photons p_T from 8GeV to 8.5GeV at the mid central collisions.

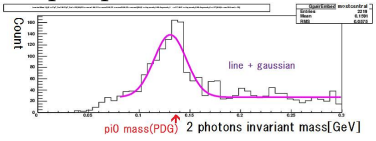

Figure 3.23: The invariant mass of two photons in the range of two photons p_T from 8GeV to 8.5GeV at the most central collisions.

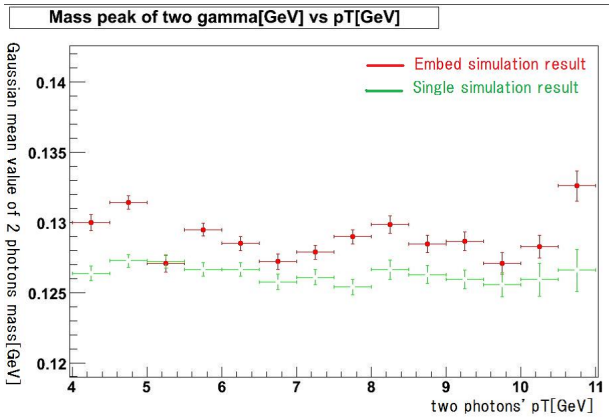

Figure 3.24: Peak position of the π^0 for the comparison between a Embedding simulation and a Single simulation.

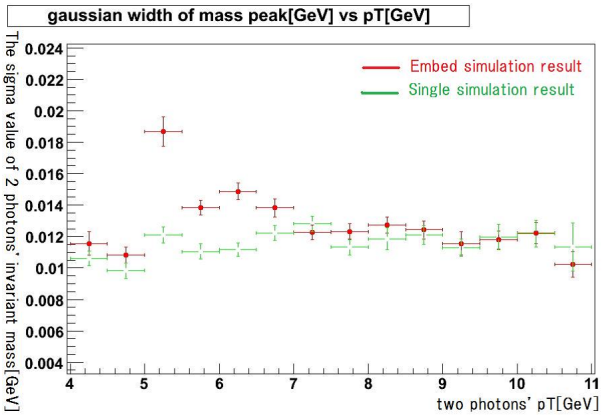

Figure 3.25: Peak width of the π^0 for the comparison between a Embedding simulation and a Single simulation.

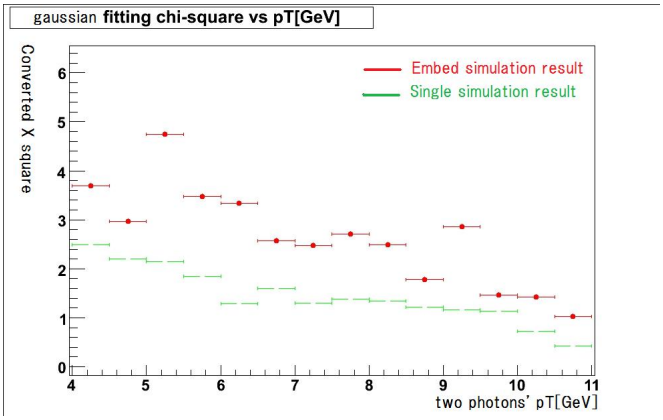

Figure 3.26: Chi square of the gaussian fitting about the mass peak of the π^0 for the comparison between a Embedding simulation and a Single simulation.

Table 3.2: The results of the fitting of the peak position and the width in two photons invariant mass distribution.

	mean mass value [GeV]	width of the mass peak [GeV]
MB	0.129417	0.0120298
0-30 % central	0.129995	0.0120902
30-60 % central	0.129198	0.0108887
60-92 % central	0.127644	0.0117368
Single simulation	0.12676	0.00949414

Secondly, I show the embeded and single results of the invariant mass distribution of 2 photons from $K^0{}_S$ for each mulitiplcity.

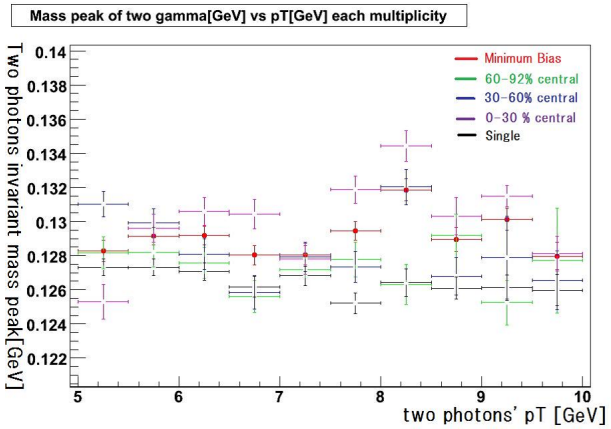

Figure 3.27: Peak position of the π^0 for the comparison between a Embedding simulation and a Single simulation.

I fit the constant in a figure3.27 and a figure3.28 to get cut-values when I calculate the four photons invariant mass and to reduce backgrounds. These results are the table3.2;

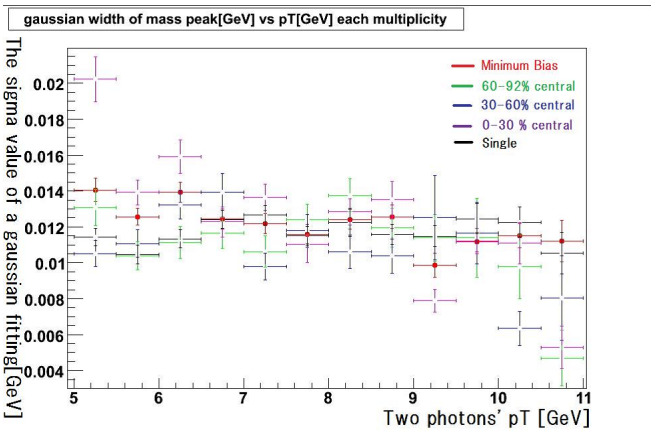

Figure 3.28: Peak width of the π^0 for the comparison between a Embedding simulation and a Single simulation.

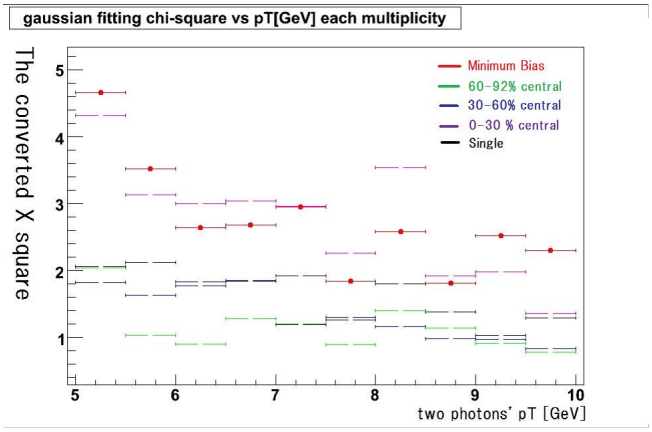

Figure 3.29: Chi square of the gaussian fitting about the mass peak of the π^0 for the comparison between a Embedding simulation and a Single simulation.

The comparison between embeded simulation and single simulation for the invariant mass distribution of 4 photons

With a π^0 mass range of the previous section, I show results of 4 photons invariant mass for each centrality and single simulation in a figure3.30, a figure3.31 and a figure3.32.

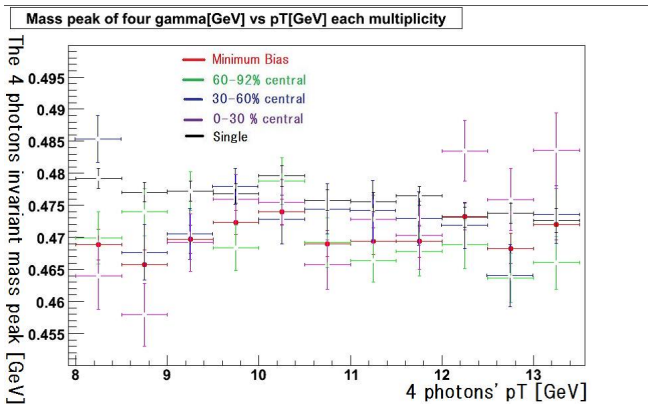

Figure 3.30: Peak position of the ${K^0}_S$ for the comparison between a Embedding simulation and a Single simulation.

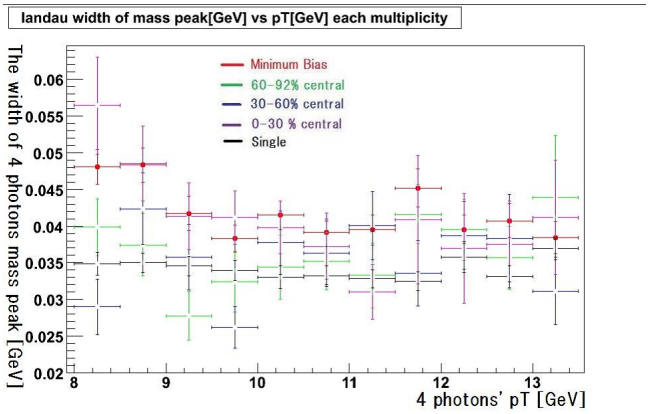

Figure 3.31: Peak width of the $K^0{}_S$ for the comparison between a Embedding simulation and a Single simulation.

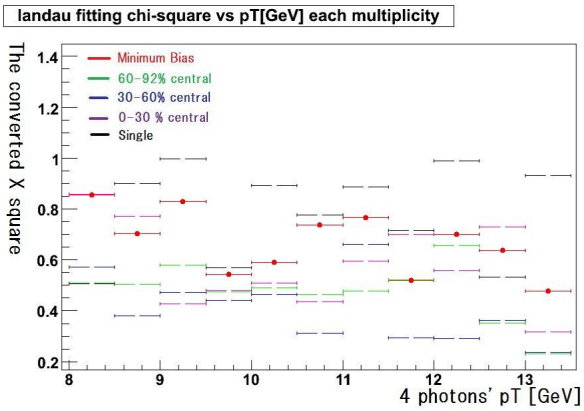

Figure 3.32: Chi square of the gaussian fitting about the mass peak of the $K^0{}_S$ for the comparison between a Embedding simulation and a Single simulation.

Chapter 4

Results and Discussion

Here, we show the results of ratios in order to lead to a conclusion. I state a effectivity of a DVL method first. Next, I show multiplcity effect of each centrality for a ${K^0}_S$ measurement. A outlook for the further analysis is discussed in the end.

4.1 Comparison between DVL analysis and normal analysis

4.1.1 Results of DVL analysis for π^0s from ${K^0}_S$

Figure4.1 and figure4.2 show mean values of 2 photons mass peak and widths of it as a transverse momentum function. DVL results agree in single simulation results within the margin of statistical error in a figure4.1 and figure4.2.

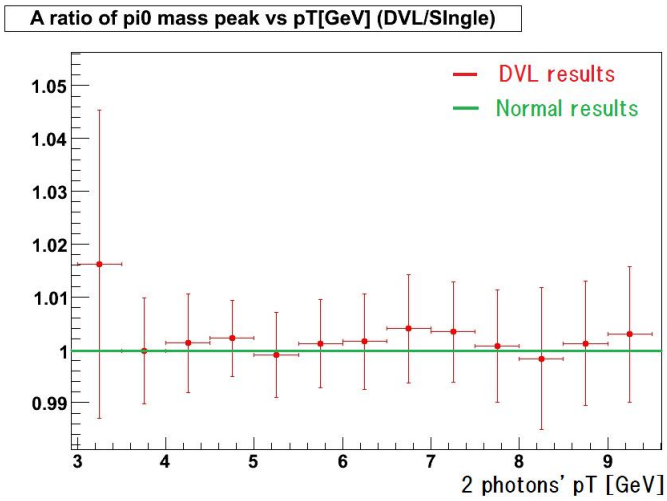

Figure 4.1: A ratio of π^0 peak from ${K^0}_S$ between DVL analysis and normal analysis as a 2 photons transverse momemtum(p_T).

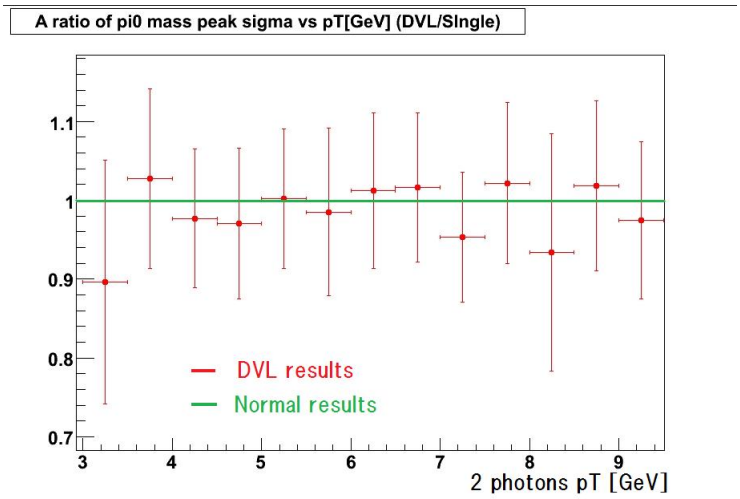

Figure 4.2: A ratio of π^0 width from ${K^0}_S$ between DVL analysis and normal analysis as a 2 photons transverse momemtum(p_T).

4.1.2 Results of DVL analysis for $K^0{}_S$

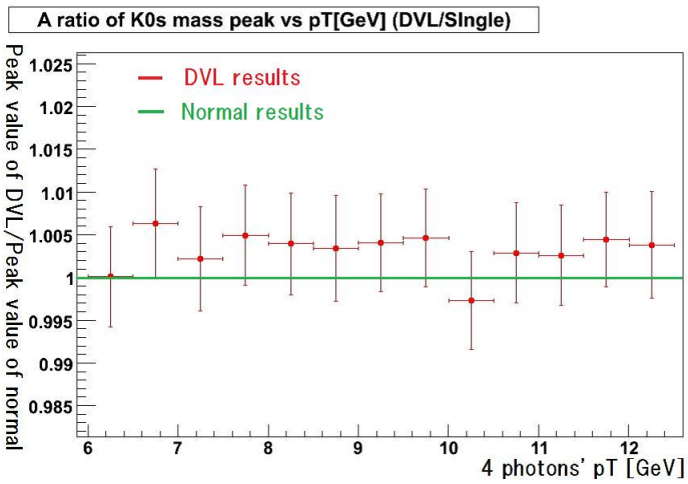

Figure 4.3: A ratio of $K^0{}_S$ peak between DVL analysis and normal analysis as a 4 photons transverse momemtum(p_T).

Figure4.3 and figure4.4 show mean values of 4 photons mass peak and widths of it as a transverse momentum function. DVL results agree in single simulation results within the margin of statistical error in a figure4.3 and figure4.4. We can't see a expected fine tune with DVL calculation even at high p_T range.

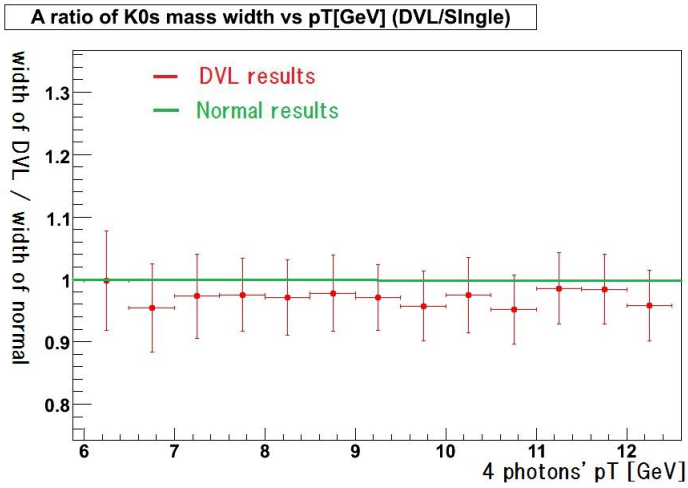

Figure 4.4: A ratio of $K^0{}_S$ peak between DVL analysis and normal analysis as a 4 photons transverse momemtum(p_T).

4.2 Multiplicity effects

4.2.1 The results of the multiplicity effects for π^0s from $K^0{}_S$

I show the ratio of π^0s' peak-values and widths in order to investigate the mulitiplicity dependence in the figure4.5 and the figure4.6.

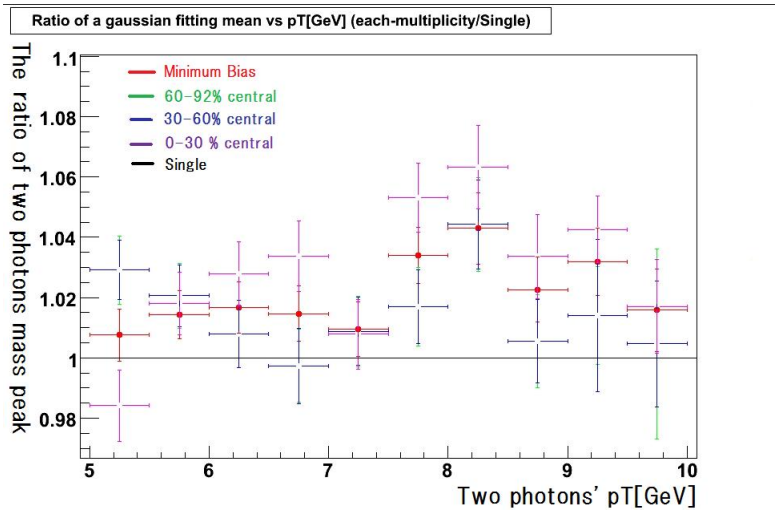

Figure 4.5: Ratio of postion of π^0 peak between embedding simulation and single simulation as a function of 2 photons pT for each centrality.

In these figures, the red plots mean the selection of the minimum bias events. Furthermore, the green plots mean the selection of 60-92 % central events, the blue plots mean the selection of 30-60 /the magenta plots mean the selection of 0-30 % central events. The mean mass values of embedding simulation are basically larger than the man values of single simulation.

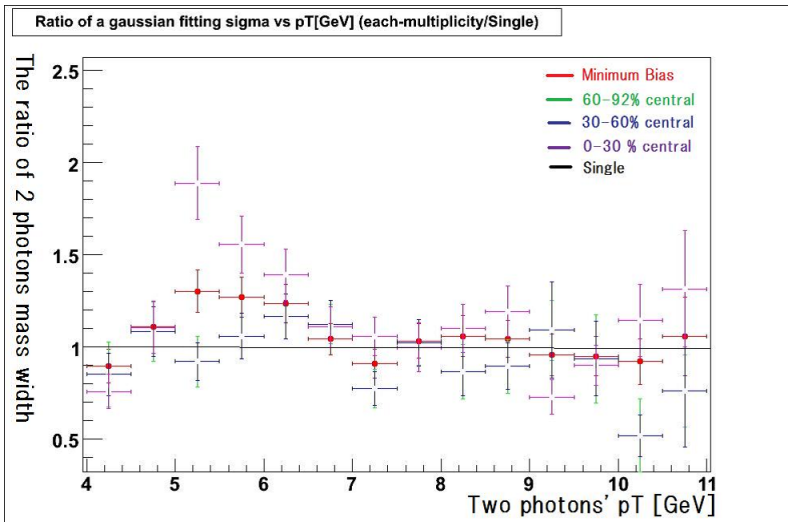

Figure 4.6: Ratio of Width of π^0 mass between embedding simulation and single simulation as a function of 2 photons pT for each centrality.

4.2.2 The results of the multiplicity effects for the $K^0{}_S$ measurement

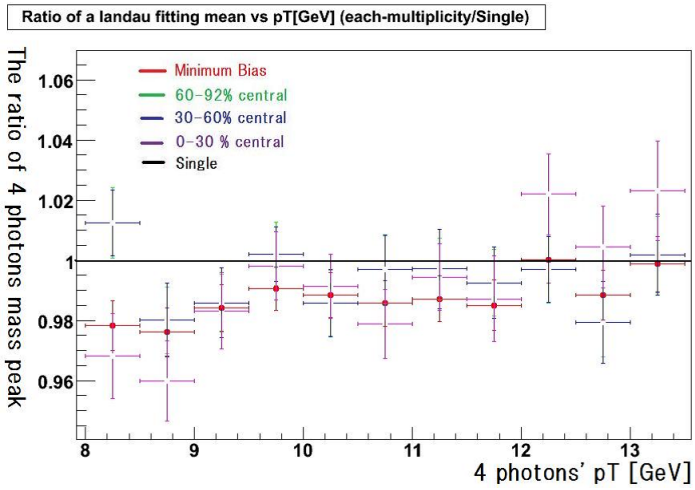

Figure 4.7: Ratio of postion of $K^0{}_S$ peak between embedding simulation and single simulation as a function of 4 photons pT for each centrality.

I show a ratio of invariant mass peak values in a figure4.7, a ratio of invariant mass width in a figure4.8. Most probable mass values of embeded simulation of each centrality agree in them of single simulation within the margin of statistical error.

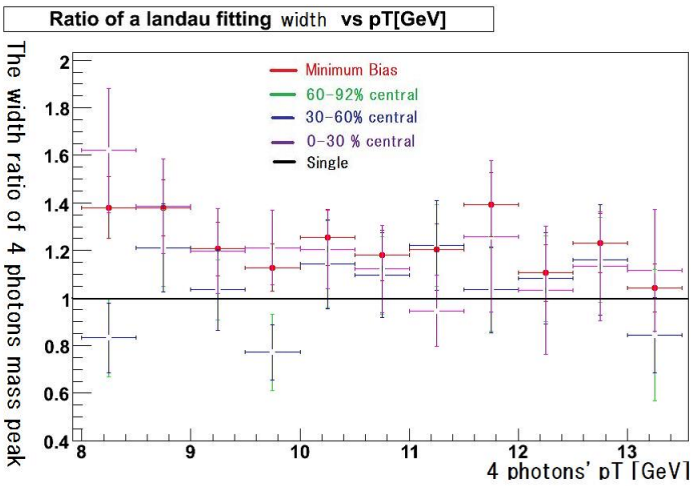

Figure 4.8: Ratio of width of $K^0{}_S$ peak between embedding simulation and single simulation as a function of 4 photons pT for each centrality.

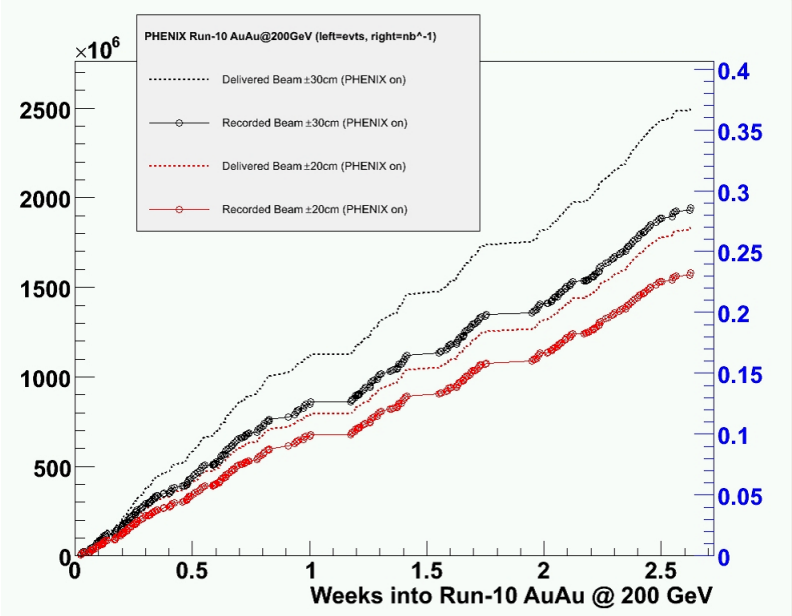

Figure 4.9: On going PHENIX integrated luminosity as a function of weeks into this-year-run[23].

4.3 Outlook

I start to analyze the this year data. I show the result of "on going" PHENIX integrated luminosity in the figure4.9. The RHIC plans a 10-weeks physics run in 2010. If we will have been just taking munimum bias data at 5 kHz flat, we would have recorded around 7.5 billion events, it is about 1.6 times the Run-7 statistics.

Chapter 5

Conclusion

We report the simulation study of signal from ${K^0}_S$ meson with photonic decay mode. We measured 2 photons invariant mass distribution of π^0 from ${K^0}_S$, and 4 photons invariant mass distribution of ${K^0}_S$ in high p_T range. In a single simulation, I discuss peak shape of 4 photon invariant mass and tried to show effectivity of the new method taking account of estimation of most probable decay vertex location(DVL). In this study, there is agreement between DVL results and normal results within the margin of statistical error. I show multiplicity effects with simulation data and data of the Au + Au collisions at $\sqrt{s_{NN}} = 200$ GeV at PHENIX experiment and the effective invariant mass range of π^0 from ${K^0}_S$ and ${K^0}_S$ for each multiplcity as a function of each particle's p_T. There is gap about 20 MeV between most probable invariant mass value of measured ${K^0}_S$ and vacuum ${K^0}_S$ mass value. At high p_T, peak distribution of 4 photons invariant mass for each centrality agrees in it of single simulation. Most statistics of Au + Au collisions are expected to be taken in 2010 and there is no reason not to analyze them.

Acknowledgement

I would like to express my gratitude to Associate Prof. Kenta Shigaki who mainly supervise this work. Also, he gave me a great chance to talk to other college students and Gabor David, who is one of the foremost researchers in the PHENIX photon analysis group. Prof. Sugitate, the boss of our laboratory gave me many chances to go to the Brookhaven National Laboratory and international conferences. I could learn not only the expert knowledge of detectors but also the physics knowledge. Those experiences had been good educations and strongly helped to elevate my motivation. Assistant Prof. Kensuke Homma gave me crucial suggestions a lot. I would like to thank Yoshihide Nakamiya, Misaki Ouchida and Kotaro Kijima for giving me precious advice and teaching some computing techniques. I wish to thank PHENIX collaboration. I'm obilged to Dr. Kyouichiro Ozawa, KEK and physics office helpers for all their help of business trip. I'm grateful to my colleages, Iwasaki Takashi, Ueki Yusuke, Chuman Fumihiro and Hiei Ayako. Finally, I express my gratitude to my spouse Nihashi Yachiyo.

Appendix A

PHENIX Coordinate System

The Z axis of the PHENIX coordinate system is defined as a direction of the beam line. The direction from the vertex point to north Muon Arm is defined as positive. The X and Y axis are defined as west direction and the vertical. The direction from the vertex point to the west Central Arm is defined as positive. The direction from the vertex point to the upward tendency is defined as positive. The angle ϕ is defined in X-Y plane as follows at (x, y, z);

$$\phi \equiv \tan^{-1} \frac{y}{x} \tag{5.1}$$

The angle θ is defined in Y-Z plane as follows at (x, y, z);

$$\theta \equiv \tan^{-1} \frac{y}{z} \tag{5.2}$$

The direction of particle is determined with ϕ and θ. In the high energy reaction, y is often used. y is called rapidity and is defined as floows;

$$y \equiv \frac{1}{2} \log \frac{E + p_z}{E - p_z} \tag{5.3}$$

where E is the energy of particle and p_z is the momentum of z-component. In the case the particle energy is large, the mass of particle is neglible. In this case,

$$y = \frac{1}{2} \log \frac{1 + p_z/E}{1 - p_z/E} \tag{5.4}$$

$$= \frac{1}{2}\log\frac{1+\cos\theta}{1-\cos\theta} \tag{5.5}$$

$$= \frac{1}{2}\log\frac{\cos^2\theta/2}{\sin^2\theta/2} \tag{5.6}$$

$$= -\log\tan\frac{\theta}{2} \tag{5.7}$$

$$\tag{5.8}$$

The pseudo-rapidity is defined as;

$$\eta \equiv -\log tan\frac{\theta}{2} \tag{5.9}$$

The rapidity y can be approximated with pseudo-rapidity η when E is enough large.

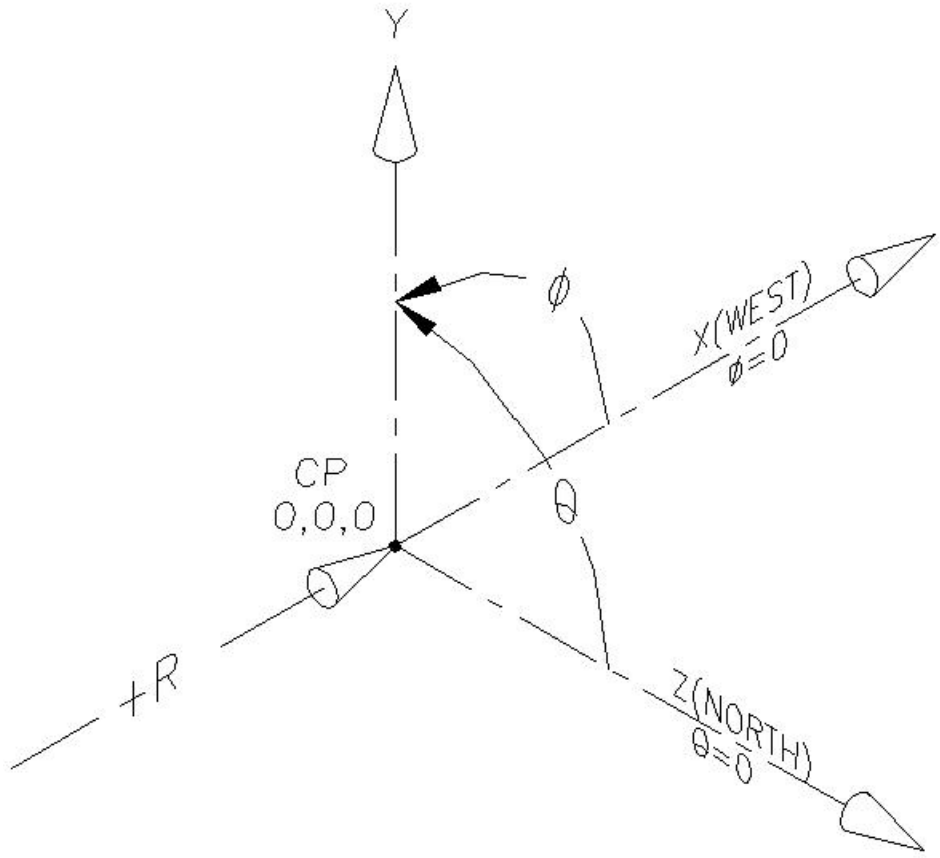

Figure 5.1: The PHENIX coordinate system[17].

Appendix B

landau function

The landau function is defined here as ;

$$\text{landau function} \equiv f(x) \equiv A \times \exp[\frac{x-C}{B} - \exp(\frac{x-C}{B})], \tag{5.10}$$

As you see this function,

$$\begin{aligned} f(x = C - 5B) &\sim 0.018 \times f(x = C) \\ f(x = C - 4B) &\sim 0.048 \times f(x = C) \\ f(x = C - 3B) &\sim 0.13 \times f(x = C) \\ f(x = C - 2B) &\sim 0.32 \times f(x = C) \\ f(x = C - B) &\sim 0.69 \times f(x = C) \\ f(x = C + B) &\sim 0.49 \times f(x = C) \\ f(x = C + 2B) &\sim 0.012 \times f(x = C) \end{aligned}$$

Then, I integrate the landau function,

$$\int_D^E A \times \exp[\frac{x-C}{B} - \exp(\frac{x-C}{B})]dx \tag{5.11}$$

I can't integrate this function mathmatically, I made a computer to calculate them. Here, I set that A is 6000, B is 0.046 and C is 0.47.

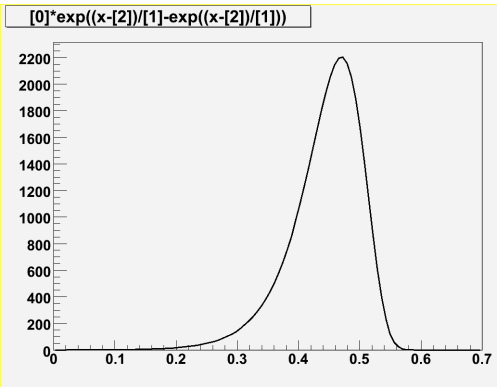

Figure 5.2: landau distribution.

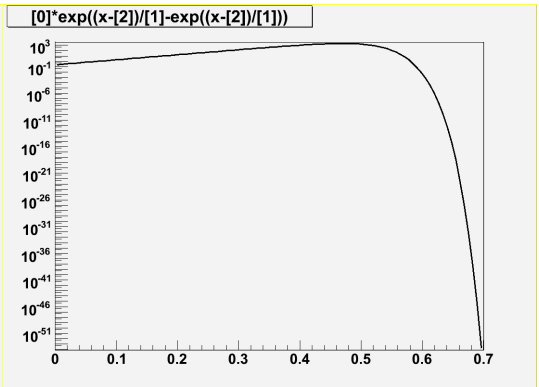

Figure 5.3: landau distribution with log scale.

D	E	$\frac{\int_D^E A\times\exp[\frac{x-C}{B}-\exp(\frac{x-C}{B})]dx}{\int_{-\infty}^{+\infty} A\times\exp[\frac{x-C}{B}-\exp(\frac{x-C}{B})]}dx$
$C-5B$	$C+3B$	0.994
$C-4B$	$C+3B$	0.982
$C-3B$	$C+3B$	0.953
$C-2B$	$C+3B$	0.875
$C-B$	$C+3B$	0.694
$C-5B$	$C+2B$	0.993
$C-4B$	$C+2B$	0.982
$C-3B$	$C+2B$	0.952
$C-2B$	$C+2B$	0.875
$C-B$	$C+2B$	0.694
$C-5B$	$C+B$	0.929
$C-4B$	$C+B$	0.918
$C-3B$	$C+B$	0.888
$C-2B$	$C+B$	0.811
$C-B$	$C+B$	0.630

Bibliography

[1] A. Bodek et al. Phys. Rev. Lett. Vol.30 Number 21 (1973)

[2] J. C. Collins and M. J. Perry Phys. Rev. Lett. Vol. 34 Number 21 (1975)

[3] F. Karsch Lecture Notes in Physics, Vol. 583, 2002, p. 209.

[4] S. Sapeta and U. A. Wiedemann, preprint, arXiv:0707.3494[hep-ph].

[5] H. L. Lai et al. (CTEQ Collaboration), Eur. Phys. J. C 12, 375(2000).

[6] S. S. Adler et al. Phys. Rev. Lett. 91 (2003) 072303.

[7] I. Arsene et al. (BRAHMS Collaboration), Nuclear Physics A (2005) 1-27.

[8] S. Albino, B. A. Kniehl, and G. Kramer, Nucl. Phys. B725, 181(2005).

[9] B. I. Abelev et al. (STAR Collaboration), Phys. Rev. C 75, 064901(2007).

[10] J. Adams et al. (STAR Collaboration), Phy. Rev. Lett. 91, 072304 (2003).

[11] W. Liu and R. J. Fries Phy. Rev. C. 77, 054902(2008).

[12] Particle data group, WWW site: http://pdg.lbl.gov/

[13] R. Averbeck. $EXODUSEventGenerator$. PHENIX CVS Repository offline/analysis/exodus

[14] R. Brun et al. GEANT Detector Description and Simulation tool, CERN Program Library Long Writeup W5013.

[15] Christian Klein-Bösing Ph. D. Thesis at University of Muenster, 2005

[16] Yoshihiro Iwanaga Master Thesis at University of Hiroshima, 2009

[17] PHENIX Official Website: http://www.phenix.bnl.gov/WWW/run/drawing/

[18] Michey Chiu Talk in the PHENIX Forcus 2004

[19] Yuji Tsuchimoto Talk in the PHENIX Forcus 2004

[20] Peter Tarjan Talk in the PHENIX Forcus 2004

[21] Martin Purschke Talk in the PHENIX Forcus 2004

[22] Experimental Quark Physics Laboratory Offical Web site: http://www.hepl.hiroshima-u.ac.jp

[23] Jamies L. Nagile Report of Run10 in phenix collaboration list